Science of the Total Environment 872 (2023) 162091

Contents lists available at ScienceDirect

Science of the Total Environment

journal homepage: www.elsevier.com/locate/scitotenv

Simultaneous profiling of dust aerosol mass concentration and optical properties with polarized high-spectral-resolution lidar

Da Xiao [a,b,1], Nanchao Wang [a,1], Sijie Chen [a], Lingyun Wu [a], Detlef Müller [c], Igor Veselovskii [d], Chengcai Li [e], Eduardo Landulfo [f], Venkataraman Sivakumar [g], Jing Li [e], Huizheng Che [h,i], Jing Fang [a], Kai Zhang [a], Binyu Wang [a], Feitong Chen [a], Xianzhe Hu [a], Xiaotao Li [a], Weize Li [a], Yicheng Tong [a], Ju Ke [a], Lan Wu [a], Chong Liu [a,b,j,k], Dong Liu [a,b,j,k,*]

[a] State Key Laboratory of Modern Optical Instrumentation, College of Optical Science and Engineering, Zhejiang University, Hangzhou 310027, China
[b] ZJU-Hangzhou Global Scientific and Technological Innovation Center, Hangzhou 311200, China
[c] School of Remote Sensing and Information Engineering, Wuhan University, Wuhan 430079, China
[d] Prokhorov General Physics Institute of the Russian Academy of Sciences, Moscow, Russia
[e] Department of Atmosphere and Oceanic Sciences, School of Physics, Peking University, Beijing 100871, China
[f] Instituto de Pesquisas Energeticas e Nucleares (IPEN), 2242 Lineu Prestes Av., Sao Paulo, SP, Brazil
[g] School of Chemistry and Physics, Discipline of Physics, University of KwaZulu-Natal, Durban 4000, South Africa
[h] State Key Laboratory of Severe Weather (LASW), Chinese Academy of Meteorological Sciences, CMA, Beijing 100081, China
[i] State Key Laboratory of Atmospheric Chemistry (LAC), Chinese Academy of Meteorological Sciences, CMA, Beijing 100081, China
[j] Intelligent Optics & Photonics Research Center, Jiaxing Research Institute Zhejiang University, Jiaxing 314000, China
[k] Jiaxing Key Laboratory of Photonic Sensing & Intelligent Imaging, Jiaxing 314000, China

HIGHLIGHTS

- First HSRL observations for profiling dust mass concentration and optical properties.
- Mass concentration and AOD from HSRL agree well with auxiliary data ($R \geq 0.9$).
- A universal analytical equation to assess dust proportion with PLDR is proposed.

GRAPHICAL ABSTRACT

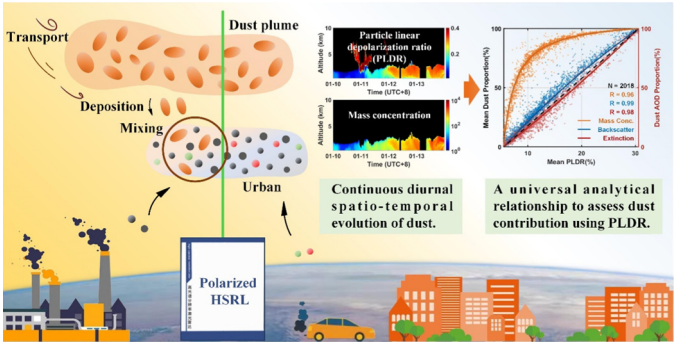

ARTICLE INFO

Editor: Jianmin Chen

Keywords:
High-spectral-resolution lidar
Dust aerosol
Particle mass concentration
Optical properties
Dust proportion

ABSTRACT

Dust particles originating from arid desert regions can be transported over long distances, presenting severe risks to climate, environment, social economics, and human health at the source and downwind regions. However, there has been a dearth of continuous diurnal observations of vertically resolved mass concentration and optical properties of dust aerosols, which hinders our understanding of aerosol mixing, stratification, aerosol-cloud interactions, and their impacts on the environment. To fill the gap of the insufficient observations, to the best of our knowledge, this work presents the first high-spectral-resolution lidar (HSRL) observation providing days of continuous profiles of the mass concentration, along with particle linear depolarization ratio (PLDR), backscattering coefficient, extinction coefficient and lidar ratio (LR), simultaneously. We present the results of two strong dust events observed by HSRL over Beijing in 2021. The maximum particle mass concentrations reached (1.52 ± 3.5) x10^3 μg/m^3 and (19.48 ±

* Corresponding author at: State Key Laboratory of Modern Optical Instrumentation, College of Optical Science and Engineering, Zhejiang University, Hangzhou 310027, China.
E-mail address: liudongopt@zju.edu.cn (D. Liu).
[1] These authors contributed equally to this work.

http://dx.doi.org/10.1016/j.scitotenv.2023.162091
Received 13 December 2022; Received in revised form 3 February 2023; Accepted 3 February 2023
Available online 08 February 2023

0.36) x10^3 μg/m^3 for the two dust events, respectively. The retrieved particle mass concentrations and aerosol optical depth (AOD) agree well with the observation from the surface PM_{10} concentrations and sun photometer with correlation coefficients of 0.90 and 0.95, respectively. The intensive properties of PLDR and LR of the dust aerosols are 0.31 ± 0.02 and 39 ± 7 sr at 532 nm, respectively, which are generally close to those obtained from observations in the downwind areas. Moreover, inspired by the observations from HSRL, a universal analytical relationship is discovered to evaluate the proportion of dust aerosol backscattering, extinction, AOD, and mass concentration using PLDR. The universal analytical relationship reveals that PLDR can directly quantify dust aerosol contribution, which is expected to further expand the application of polarization technology in dust detection. These valuable observations and findings further our understanding of the contribution of dust aerosol to the environment and help supplement dust aerosol databases.

1. Introduction

Aerosols play an important role in the Earth's radiation budget and the global climate via scattering and absorbing solar radiation (direct effect), serving as nuclei for cloud formation to modify cloud microphysical properties and precipitation efficiency (indirect effect) (Creamean et al., 2013; Toll et al., 2019). Especially dust aerosols, which account for ~35 % of the total aerosol mass (IPCC, 2013), are the most abundant aerosol types in the atmosphere (IPCC, 2021). Dust particles originating from arid desert regions can be transported over long distances through strong winds, thus presenting severe risks to climate, environment, socioeconomics, and human health at the sources and downwind regions (Liang et al., 2022; Uno et al., 2009). They also provide most of the iron in the oceans when being transported from the land through the atmosphere to the oceans, affecting ocean biogeochemistry and helping drive the biogeochemical cycles of the earth (Jickells et al., 2005; Zhang et al., 2023).

Despite ground-based in situ instruments and the Aerosol Robotic Network (AERONET) that gather information on particle mass concentrations and aerosol optical properties of dust (Che et al., 2019; Dubovik et al., 2002), our knowledge of the vertical distribution of dust remains insufficient. This lack of knowledge hinders the investigation of details of aerosol mixing and stratification processes, long-distance transport, and aerosol-cloud interactions, which therefore leads to significant uncertainty in environmental and climate models (Adebiyi and Kok, 2020; Binietoglou et al., 2015; Gandham et al., 2022). Lidar can gather the vertical structure of aerosols and clouds with high spatial-temporal resolution in near real-time, thus making this technology a powerful tool for dust aerosol detection (Chen et al., 2022; Engelmann et al., 2016; Hair et al., 2008).

Mie scattering lidar, such as Cloud-Aerosol Lidar with Orthogonal Polarization (CALIOP), requires the assumption of the lidar ratio as input when evaluating aerosol backscattering and extinction coefficient, which introduces considerable uncertainty (Kim et al., 2018; Omar et al., 2009). Advanced lidars, such as Raman lidar (RL) and high-spectral-resolution lidar (HSRL), can retrieve high-precision optical properties independently without critical assumptions, which played an important role in acquiring the characteristics of dust aerosols. Heretofore, field missions equipped with RLs or HSRLs have been carried out to acquire comprehensive datasets of Saharan dust (Groß et al., 2015; Veselovskii et al., 2016), North American dust (Burton et al., 2012) and Asian dust (Hofer et al., 2017; Tatarov et al., 2012). However, these observations mainly focus on the optical properties of dust aerosols. Only a few observations with RLs provide the mass concentration simultaneously, reflecting aerosol load. Meanwhile, there has been a dearth of continuous diurnal observations of vertical-resolved mass concentration and optical properties of dust aerosols due to the insufficient signal-to-noise (SNR) with RLs during daytime. Simultaneous observation of mass concentration and optical properties of dust aerosol are essential for quantifying the contribution of dust aerosols to the environment as dust aerosols are usually mixed with other aerosols, especially in downwind areas. Especially the continuous diurnal observations would further contribute to our understanding of the complete spatiotemporal evolution of dust aerosols, thus reducing uncertainties in model predictions. HSRL has a better SNR in the daytime, which can provide the diurnal observations of vertical-resolved mass concentration and optical properties of dust aerosols (Ke et al., 2022; Wang et al., 2022a). Thus, comprehensive investigations of dust aerosol optical properties and mass concentration with HSRL are urgently needed to promote studies of aerosol classification, mixing processes of dust aerosols with local aerosols, and quantification of dust aerosol contribution to the environment.

This paper, to the best of our knowledge, reports the first HSRL observations providing days of continuous profiles of mass concentration, along with particle linear depolarization ratio (PLDR), backscattering coefficient, extinction coefficient, and lidar ratio (LR) of dust aerosols simultaneously. The results for two representative dust pollution events measured by the HSRL developed by Zhejiang University (ZJU-HSRL) over Beijing in 2021 are presented. To verify the rationality of the results, we compare the results from ZJU-HSRL observations with surface PM_{10} concentrations and the results from sun photometers. The comparisons show acceptable consistency. Furthermore, we compare the LR and PLDR of dust aerosols obtained from HSRL to those obtained from historical RL observations carried out at other sites. The comparison shows that values on average are close. Finally, inspired by the observation results, a universal analytical relationship of PLDR and dust optical properties and mass concentration proportion is investigated to directly characterize the contribution of dust aerosols to the overall aerosol load. These valuable observations could contribute to supplementing the dust aerosol databases, which were lacking in previous studies and climate model studies.

The remainder of the paper is organized as follows. The optical properties and mass concentration obtained by ZJU-HSRL and other auxiliary data for comparison are presented in Section 2. Section 3 presents the spatiotemporal variation of two representative dust events obtained by ZJU-HSRL and comparative analysis results. Finally, a conclusion is given in Section 4.

2. Materials and methodology

2.1. Dual-field-of-view polarized HSRL

The dual-field-of-view polarized HSRL (Wang et al., 2022b) developed by Zhejiang University performed continuous cloud and aerosol observations in Beijing from November 2020 to March 2021. During the study period, besides the urban aerosols caused by human activities, Beijing was affected by dust aerosols transported from the Taklimakan Desert in western China and the Gobi Desert. This atmospheric situation provided a unique opportunity to study the properties of dust aerosols (Cao et al., 2014; Yu et al., 2017). The locations of ZJU-HSRL and instruments used for taking auxiliary data are shown in Fig. 1 (a). Fig. 1 (b) is a photo of ZJU-HSRL on the campus of Peking University. Details of the observation site and measurement time of the ZJU-HSRL are listed in Table S1 in the Supplementary Information (SI).

ZJU-HSRL system employs the HSRL technique at 532 nm based on the iodine filter. The system is equipped with a frequency-doubled Nd: YAG laser with 100 mJ output and 10 Hz repetition frequency (Jiang et al., 2022; Zhang et al., 2022). The Glan-laser polarizer is used to ensure that high polarization purity of the emitted laser light is achieved. The echo signals from aerosols/clouds are collected by the telescope and detected by photomultiplier tubes or avalanche photodiode detectors (Jia et al., 2020; Li et al., 2020; Sun et al., 2022). The receiving system includes four

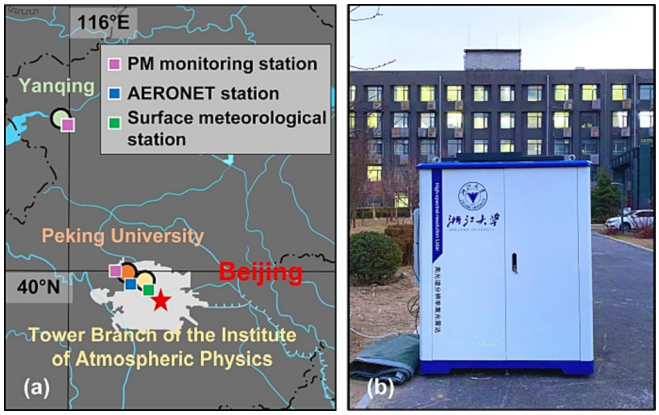

Fig. 1. (a) The locations of ZJU-HSRL and the instruments used for collecting auxiliary data in Beijing during the field experiment. The circles represent the sites of ZJU-HSRL, i.e. Yanqing (green), Peking University (orange), and the Tower Branch of the Institute of Atmospheric Physics (yellow). The squares in purple, blue, and green denote the PM monitoring station, AERONET station, and surface meteorological station, respectively. (b) A photo of ZJU-HSRL on the campus of Peking University. (For interpretation of the references to colour in this figure legend, the reader is referred to the web version of this article.)

channels, i.e., combined parallel, combined perpendicular (polarization channel), and two field-of-view parallel molecular channels. The relative calibration factor of the combined parallel and perpendicular channels is determined with the $\pm 45^{o}$ calibration method (Freudenthaler et al., 2009) and the obtained polarization ratio can distinguish between non-spherical particles and spherical particles. The additional well-designed near-range channel receives a wide-field-of-view molecular signal which is used to calibrate the incomplete overlap function and multi-scattering effects that usually occur in the context of water cloud retrievals (Shen et al., 2020; Wang et al., 2022b). The lowest height at which the overlap function of the wide-field-of-view channel equals 1 is about 200 m above the lidar. The sampling frequency of the lidar detection system is 20 MHz, and the corresponding spatial resolution is 7.5 m. To facilitate unifying the data format, the temporal resolution of the signal is 5 min in this study unless otherwise specified. Detailed information about the ZJU-HSRL can be found in our previous work (Wang et al., 2021a; Wang et al., 2022b). By the way, only the single-scatter lidar equation is considered in this study.

Combining the backscattering signals measured by these channels, two intensive aerosol properties, i.e. the particle linear depolarization ratio δ_a, and the lidar ratio S_a can be derived

$$\delta_a = \frac{R\delta(\delta_m + 1) - \delta_m(\delta + 1)}{R(\delta_m + 1) - (\delta + 1)}, \tag{1}$$

$$S_a = \frac{\alpha_a}{\beta_a}. \tag{2}$$

where, δ_m represents the depolarization by molecules. δ denotes the volume depolarization ratio which can be directly obtained using the combined parallel and perpendicular signals. R, α_a and β_a are the scattering ratio, extinction coefficient, and backscattering coefficient of aerosols, respectively. The derivations of these parameters and the corresponding uncertainties were discussed in detail in previous studies (Cheng et al., 2014; Liu et al., 2019; Xiao et al., 2020).

Subsequently, the feature detection method is employed to distinguish aerosols from clouds. The method is based on the optical aerosol properties obtained by ZJU-HSRL (Wang et al., 2021a). Compared to aerosols, clouds typically show stronger backscattering, lower lidar ratio, higher attenuation, and steeper gradients at layer boundaries, e.g. transitions from cloud-free or aerosol to cloud regions. Therefore, aerosols can be separated from clouds using an empirical threshold of the scattering ratio and LR. The classification of aerosols is realized by the use of the intensive aerosol properties PLDR and LR. These parameters vary with the aerosol type and do not depend on aerosol concentration. Three main types of aerosols are considered in this study: dust, polluted dust, and urban. It is worth noting that smoke and urban aerosols are not distinguished in this study as the main task is to separate dust from all else. The characteristic values of PLDR and LR for aerosol classification follow previous work (Bohlmann et al., 2018; Burton et al., 2012; Groß et al., 2013).

The polarization lidar photometer networking (POLIPHON) method is applied to separate dust backscattering and retrieve particle mass concentration profiles (Ansmann et al., 2012; Tesche et al., 2009). Assuming a two-type mixture of dust and urban aerosols (Ansmann et al., 2019), the backscattering coefficient of the dust β_d is expressed as

$$\beta_d = \beta_a \frac{(\delta_a - \delta_{nd})(1 + \delta_d)}{(\delta_d - \delta_{nd})(1 + \delta_a)}, \tag{3}$$

where β_a and δ_a are the backscattering coefficient and PLDR, respectively, of aerosols retrieved by HSRL. δ_d and δ_{nd} are the typical PLDR values of dust and urban. It is worth noting that, if $\delta_a < \delta_{nd}$, we set $\beta_d = 0$. On the contrary, if $\delta_a > \delta_d$, we set $\beta_d = \beta_a$. The backscattering coefficient of urban aerosols can be easily calculated using $\beta_{nd} = \beta_a - \beta_d$. We estimate the profiles of the extinction coefficients α_d and α_{nd} for dust and non-dust aerosols by multiplying β_d and β_{nd} with the respective values of LR S_{nd} and S_{nd}, all of which can be determined by ZJU-HSRL observations. The statistical characteristics of urban/smoke aerosols from hourly averaged results during the study period are $\delta_{nd} = 0.055 \pm 0.018$ and $S_{nd} = 57 \pm 12$ sr, both of which are obtained by limiting the PLDR to <0.08. Following the results of (Groß et al., 2013), the PLDRs of dust aerosols are selected to be larger than 0.28 and the corresponding typical characteristics are $\delta_d = 0.306 \pm 0.015$ and $S_d = 41 \pm 6$ sr.

Then particle mass concentration of dust m_d and urban m_{nd} can be estimated as

$$m_d = \rho_d \left(\overline{v_c/\tau_c}\right) \alpha_d, \tag{4}$$

$$m_{nd} = \rho_{nd} \left(\overline{v_f/\tau_f}\right) \alpha_{nd}, \tag{5}$$

where, $\rho_d = 2.6g \cdot cm^{-3}$ and $\rho_{nd} = 1.6g \cdot cm^{-3}$ (Ansmann et al., 2012) are the density of dust and urban, respectively. v and τ represent the volume concentration and AOD obtained by solar photometers. The subscripts c and f denote coarse and fine mode, respectively. By evaluating several years of sun photometer measurements at the Beijing_CAMS site, we get $\overline{v_f/\tau_f} = 0.126$ μm. With the restriction of AE < 0.3 (440/870 nm) and AOD > 0.1 at 532 nm (Ansmann et al., 2019), we get $\overline{v_c/\tau_c} = 1.08$ μm, which is consistent with the value reported by (Zheng et al., 2021). The related input parameters involved in the algorithm are summarized in Table S2 in SI.

The uncertainties of the retrieved particle mass concentration mainly include two parts (Tesche et al., 2009; Wang et al., 2021b): (1) the uncertainties of the retrieved backscattering coefficient and PLDR, which mainly depend on the signal-to-noise ratio of lidar backscattering signals, and (2) the uncertainties of the input parameters in Table S2 in SI. The uncertainties of the PLDR and backscattering coefficient retrieved by ZJU-HSRL are 2–10 %. The uncertainties of the backscattering coefficient, extinction coefficient, and particle mass concentration profiles of the separated dust and urban could be further estimated by the law of error propagation. Combining the uncertainties of the PLDRs, LRs, mass densities, and conversion factors of urban and dust aerosols, the uncertainty of particle mass concentration is 30 % ~ 50 %.

2.2. Auxiliary data

2.2.1. Near-surface air pollutant concentrations

The hourly $PM_{2.5}$ and PM_{10} concentrations near the ground have been monitored by the China National Environmental Monitoring Center since

the end of 2012 (Wei et al., 2021). The $PM_{2.5}$ and PM_{10} concentrations are collected from the Beijing Municipal Ecological and Environmental Monitoring Center (http://www.bjmemc.com.cn/, accessed 7th January 2022). The data are used to investigate the impact of dust aerosols. The Yanqing monitoring station (40.45°N, 115.97°E) is chosen for comparison of data taken in November. The station is about 10 km from ZJU-HSRL at the Yanqing site. For data taken between December 2020 and April 2021, the Haidian Wanliu monitoring station was selected. This station is <10 km from Peking University and the Tower Branch of the Institute of Atmospheric Physics.

2.2.2. AERONET aerosol optical depth products

The Aerosol Robotic Network of identical globally distributed sun and sky-scanning ground-based automated radiometers provides measurements of aerosol optical properties (Holben et al., 1998). In this study, AOD at 500 nm obtained by interpolation and the Ångström exponent (AE) between 440 and 870 nm from the Beijing_CAMS site (39.93°N, 116.32°E) are utilized to evaluate the results from lidar measurement.

2.2.3. Meteorological data

The surface wind speed and relative humidity are taken from a monitoring station (39.91°N, 116.38°E, see https://www.timeanddate.com/weather/china/beijing, accessed 1st March 2022) about 10 km away from Peking University and Tower Branch of the Institute of Atmospheric Physics.

2.2.4. HYSPLIT backward trajectory

Hybrid Single Particle Lagrangian Integrated Trajectory (HYSPLIT) is a professional model developed by the US National Oceanic and Atmospheric Administration (NOAA) and the Australian Meteorological Administration to calculate and analyze the transport and diffusion trajectories of atmospheric pollutants (Stein et al., 2015). In this study, the HYSPLIT model of the National Center for Environmental Prediction (NCEP) GDAS data product is employed to calculate the 48-h air mass backward trajectories and explore possible sources of the aerosols observed in our research work.

3. Results and discussion

3.1. General overview of observation

During the study period, dust plumes from the arid desert were transported to Beijing by the prevailing northwest wind, which led to multiple dust pollution events. The time series of daily averaged AOD at 500 nm and Ångström exponent (440/870) obtained by AERONET over Beijing from November 2020 to April 2021 are presented in Fig. 2 (a). The monthly averaged AOD is from 0.3 to 0.4 from November 2020 to February 2021 while it increased significantly in March and April and reached a maximum value of 0.94 in March. The Ångström exponent (440/870) varied between 0.5 and 1.5 with an average of 1.01 ± 0.37, indicating that particles in the fine mode were the major component of atmospheric aerosols during that time. The lowest monthly averaged Ångström exponent (440/870) appeared in March. The percentage of observation days in which the Ångström exponent (440/870) <0.5 is 38.1 % (8/21). The negative correlation between AOD and Ångström exponent (440/870) indicates that Beijing was significantly affected by dust aerosols, especially in March, and coarse dust particles are primarily responsible for the strengthening of AOD. Surface PM_{10} concentration is much higher than surface $PM_{2.5}$ concentration and $PM_{2.5}$/ PM_{10} ratio is small when the Ångström exponent (440/870) is low as shown in Fig. 2 (b), which supports the aforementioned viewpoint well.

To better illustrate the impact of dust aerosols as well as their pollution process in the context of the dust event, two representative cases are selected during the study period. One is the event of dust-aerosol intrusion into the boundary layer recorded at the Peking University site from 10 to 13 January 2021. The other case is an extreme dust event observed at the Tower Branch of the Institute of Atmospheric Physics from 15 to 18

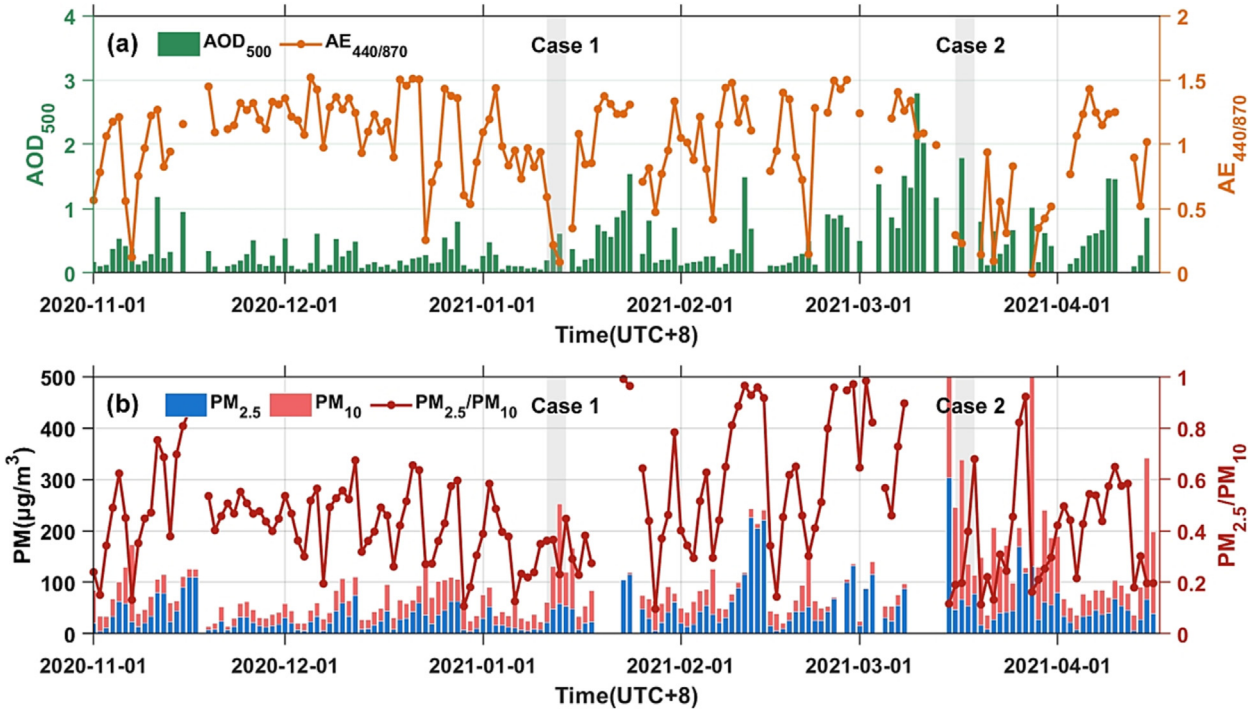

Fig. 2. The observation of (a) daily averaged AOD at 500 nm and Ångström exponent (440/870) from AERONET, and (b) daily averaged $PM_{2.5}$, PM_{10} and $PM_{2.5}$ /PM_{10} ratio at the surface. The shaded areas represent the time of the representative cases with low Ångström exponent (440/870), high PM_{10} concentration, and available ZJU-HSRL observations.

March 2021. The Ultraviolet Aerosol Index (UVAI) of two dust events is presented in Fig. S1 in SI.

3.2. Case study

3.2.1. Case 1: dust-aerosol intrusion boundary-layer event, January 10 to 13, 2021

From January 10 to 13, 2021, a significant increase in the UVAI value can be observed in the Beijing area, as portrayed in Fig. S1 in SI. The overall UVAI in the displayed range was small from January 10 to 11 and the UVAI was <0 in Beijing. A strong dust plume appeared in western Inner Mongolia on January 12 and the UVAI around Beijing reached a maximum of ~3.18 on January 13, indicating that dust aerosols gradually accumulated and dominated. Meanwhile, the Ångström exponent (440/870) obtained from the sun photometer observations decreased from 0.94 on January 10th to a minimum value of 0.083 on January 13th. During this period, surface $PM_{2.5}$ concentration remained below 60 μg/m^3, while PM_{10} concentration increased significantly, reaching 252 μg/m^3 on the 13th. The trend of these parameters is coincident with the variation of UVAI, which sufficiently proves that large dust particles became the main contributors to the atmospheric components over Beijing during this period.

The dust event was recorded by ZJU-HSRL at the Peking University site. Fig. 3 (a)-(f) presents the evolution of backscattering, PLDR, extinction, LR, feature classification, and mass concentration, respectively. The areas in white represent the downtime of the system due to rain and system adjustments. The observed case includes two layers: the bottom aerosol layer and the upper cloud layer. It is noticed that the backscattering, extinction, PLDR, and mass concentration increase with time, indicating that the enhancement of aerosol loading and the non-spherical dust aerosol gradually became the dominant contributor to the overall aerosol load. The feature classification results in Fig. 3 (d) show the change of aerosol type from urban to dust aerosols as well. Urban was the main contributor on 10th January, whose LR and PLDR at 532 nm are 45 ± 14 sr and 0.07 ± 0.03, respectively. Subsequently, the scattering ratio and PLDR of the aerosols in the bottom layer increased continuously, while LR decreased slightly. The aerosol type on January 11th was polluted dust. The PLDR increased to >0.28 after 6:00 (UTC + 8) on 12th January, indicating the predominance of dust aerosol. The LR and PLDR of dust aerosols are 39 ± 7 sr and 0.31 ± 0.02, respectively. Since the dust was transported from external sources, the enhancement of the optical properties such as scattering ratio and PLDR first appeared at the top of the boundary layer and then affected the surface. On January 13th, HSRL again observed this process which was likely due to the continuous injection of dust aerosol. The aerosol vertical structure generally presented a double layer of upper dust and bottom polluted dust. Due to the mixing of urban aerosol, the PLDR of polluted dust remained relatively low. Meanwhile, the boundary layer height determined by ZJU-HSRL increased from ~1.6 km to >2.5 km during this period due to the influence of dust aerosols. The boundary layer height could be retrieved by the wavelet covariance transform method with maximum limited height initialization and range restriction technique (Zhong et al., 2020). This finding is consistent with the results of radiosonde data, as shown in Fig. S2 in SI. These discoveries indicate that, with the capability to resolve the vertical structure of aerosol plumes, HSRL can follow the spatiotemporal evolution process of dust events. Also, HSRL can observe continuous

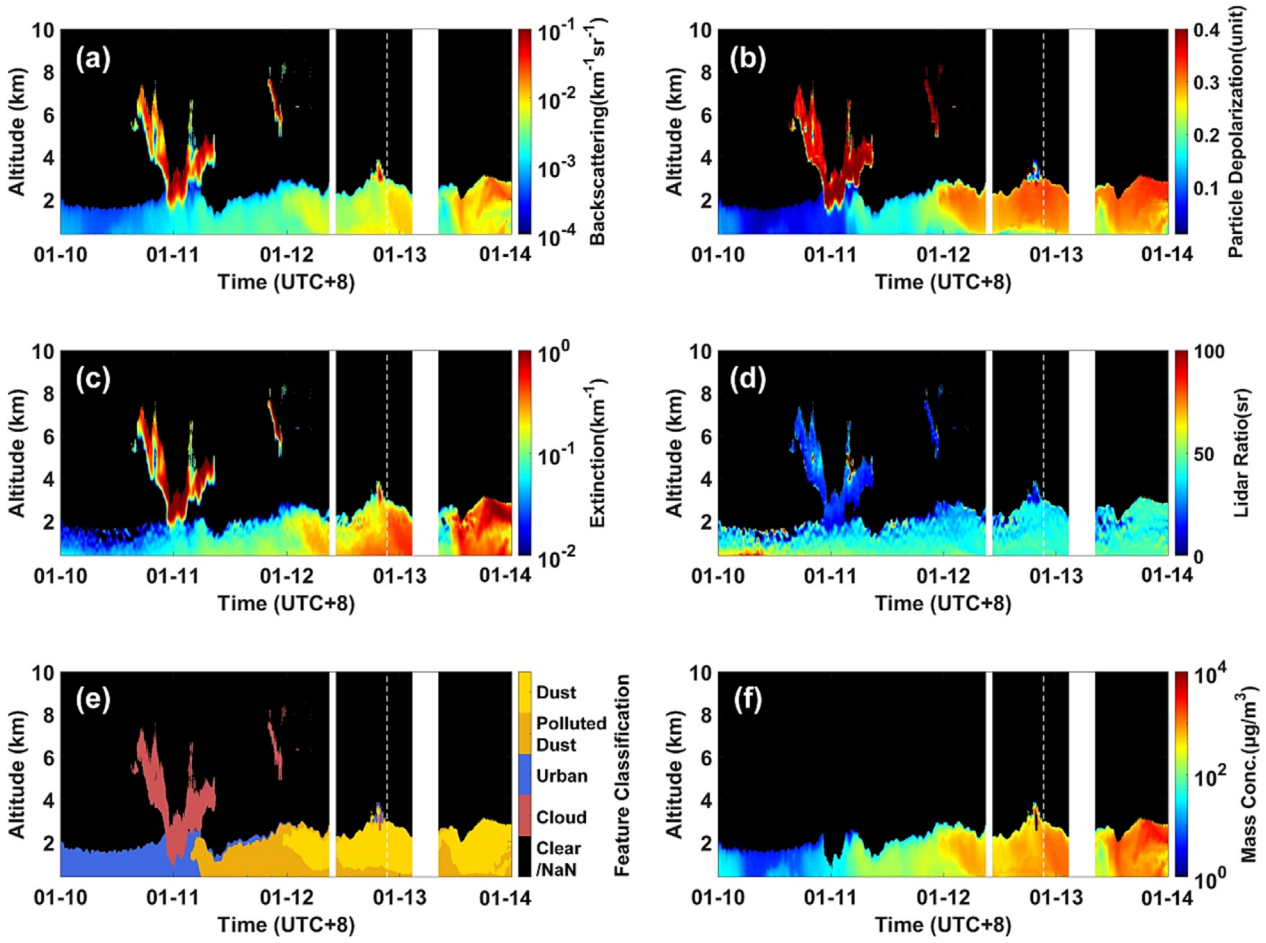

Fig. 3. Optical properties and mass concentration measured by ZJU-HSRL at Peking University from January 10 to 13, 2021. (a) backscattering, (b) particle linear depolarization ratio, (c) extinction, (d) lidar ratio, (e) feature classification, and (f) mass concentration. The areas in white are the downtime of the system due to rain and system adjustments. The dotted white lines are shown in Fig. 4.

diurnal changes in the dust transport process, which provides strong support for further understanding of the influence and mixing process of dust aerosols.

To illustrate the vertical structure of the aerosols observed in our study, the profiles of aerosol backscattering coefficient, extinction coefficient, PLDR, LR, and mass concentration observed by ZJU-HSRL at 21:20 (UTC + 8) on January 12, 2021, are presented in Fig. 4 (a)-(e) in which the error bars represent the standard deviation. The apparent double-layer aerosol structure consists of an upper layer that typically contains dust aerosol and a bottom layer that usually is made up of polluted dust. The vertical structure of PLDR reflects the proportion of dust aerosols which increases gradually with height. Values of PLDR are about 0.21 ± 0.02 below 0.5 km and strengthen to 0.32 ± 0.01 above 1 km. The vertical distribution of the backscattering coefficient indicates that the largest dust loading appeared at 2.4 km and dropped slightly with decreasing height. Due to the contribution of urban aerosol, the backscattering increases again in the polluted dust layer. The extinction coefficient shows a different variation trend, i.e. it decreases with height. Therefore, although the LR profile keeps relatively stable throughout the profile, it shows a slight difference in the polluted dust and dust layers, with values of 45 ± 2 sr and 39 ± 4 sr, respectively. The dust mass concentration in Fig. 4 (e) is derived by Eq. (4) (Ansmann et al., 2012) with the corresponding parameters summarized in Table S2 in SI, and the results of this method have been widely verified by airborne in situ observations in previous studies (Bravo-Aranda et al., 2015; Mamali et al., 2018). The high dust mass concentration (>500 μg/m^3) indicates the existence of strong dust aerosol loading along the whole profile, which further illustrates the important impact of dust aerosol on the air quality in Beijing.

Fig. 4 (f) presents the 48-h backward trajectories of HYSPLIT at 10:00 (UTC) on January 12th, where the red, blue, and green lines represent the tracking heights of 1000, 1500, and 2000 m above ground level, respectively. The backward trajectories arriving on January 12th show that the dust aerosol was transported from the Kazakhstan desert and through the Gobi Desert to the observation site, and the transmission paths of trajectories at different heights are almost the same. The backward trajectories illustrate the source of dust aerosols intuitively and confirm the ZJU-HSRL observation in Fig. 3.

The time series of ZJU-HSRL observations and surface auxiliary data for the studied case are shown in Fig. 4 (g)-(j). The surface wind speed in Fig. 4 (g) shows that the high wind speed before January 12th promoted the transport of exogenous aerosols to the observation site. Subsequently, the wind speed lowered to <5 km/h and the unfavorable dispersion conditions facilitated the accumulation of pollutants. The relative humidity remained low during the period. The AOD obtained by the sun photometer in Fig. 4 (h) and the surface PM_{10} concentration in Fig. 4 (i) increased to 1.0 and 468 μg/m^3 on the 13th, respectively. These numbers showed significant

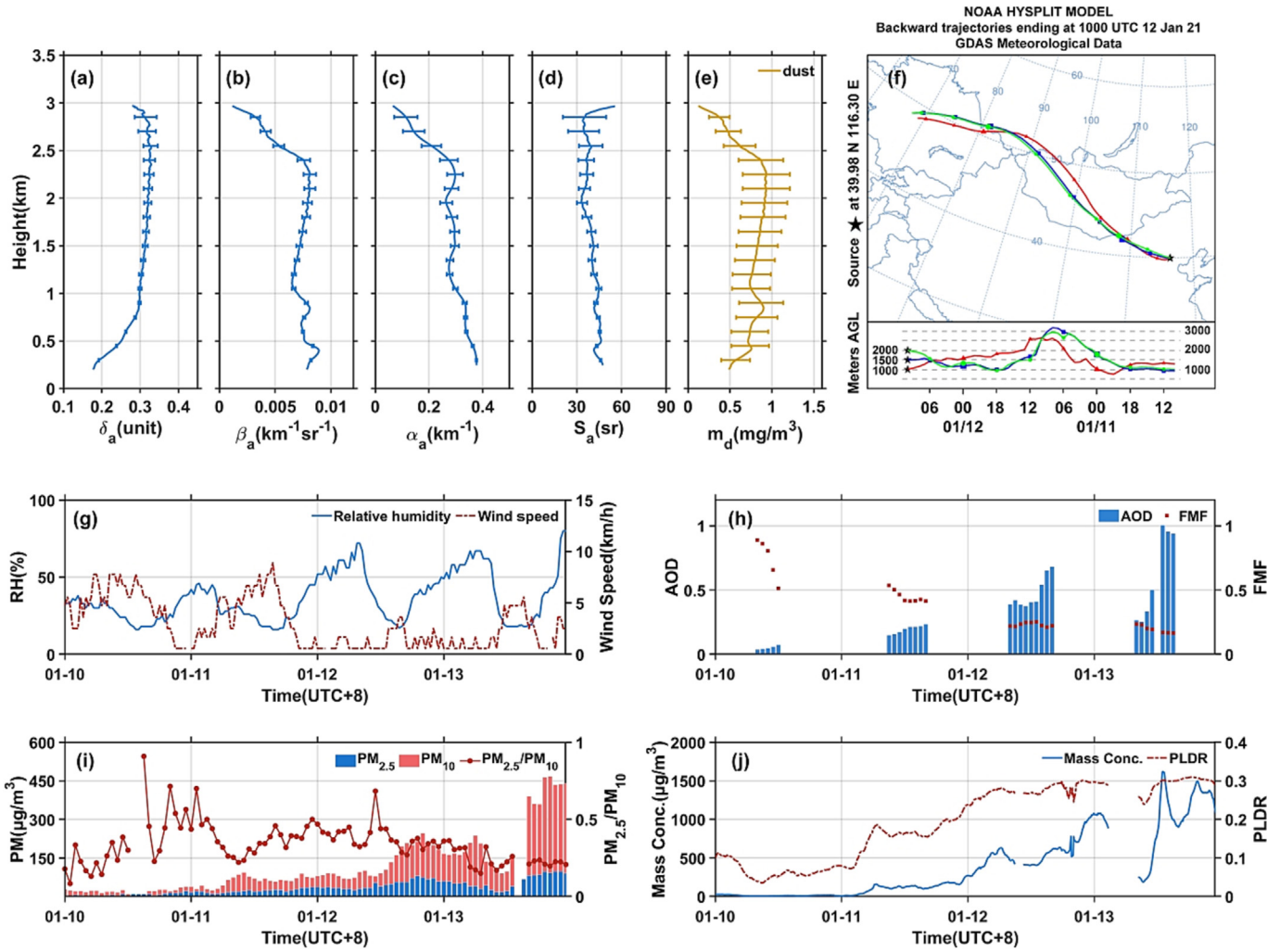

Fig. 4. Profiles of (a) PLDR, (b) backscattering, (c) extinction, (d) lidar ratio, and (e) mass concentration at 21:20 (UTC + 8) on January 12 (dotted line in Fig. 4). (f) 48 h HYSPLIT backward trajectories at Peking University at 10:00 (UTC) at 1000 m (red), 1500 m (blue), and 2000 m (green) above ground level. The time series of (g) relative humidity and wind speed, (h) AOD and FMF from AERONET, (i) $PM_{2.5}$, $PM_{10,}$ and $PM_{2.5}$ /PM_{10} ratio, and (j) mean particle mass concentration and mean PLDR obtained by ZJU-HSRL. (For interpretation of the references to colour in this figure legend, the reader is referred to the web version of this article.)

agreement with the observation results obtained with ZJU-HSRL, see Fig. 4 (j). We find a low value of the column-averaged mass concentration (<30 μg/m^3) from HSRL on January 10th. The mass concentration increased to 268 ± 129 μg/m^3 at 00:00 (UTC + 8) on 12th January when dust aerosols were first observed at the top of the boundary layer (see Fig. 3 (d)), and then reached a maximum of (1.52 ± 0.35) x10^3 μg/m^3 at 13:20 (UTC + 8) on 13th January. The $PM_{2.5}$ /PM_{10} ratio fluctuates significantly on 10th January, which could be accounted for by the relatively low aerosol loading (PM_{10} < 30 μg/m^3). The fine mass fraction (FMF) is >0.5, indicating the dominance of fine-mode urban aerosols during this period. With time, the $PM_{2.5}$/PM_{10} ratio and the corresponding FMF decreased to ~0.2, illustrating the gradual accumulation of coarse mode aerosols, which corroborates the variation of PLDR with the observation time of ZJU-HSRL. On the 13th, the absence of ZJU-HSRL data from 3:00 to 8:00 (UTC + 8) and the low PLDR observed at 9:00 (UTC + 8) may be attributed to rainfall. Then the values of AOD, surface PM_{10} concentration, and mass concentration increased again with the strengthening of the wind speed because wind acts as the driving force of dust events (Lv et al., 2020; Yin et al., 2021).

It is worth noting that the change of the AOD as observed by AERONET and lidar was almost synchronous. In contrast, the variation of the data obtained from the surface PM_{10} monitoring station is lagging the remote sensing data by about 6 to 16 h. That delay could be attributed to two reasons. (1) Dust aerosols are transported from external sources and first appear at the top of the boundary layer. (2) The monitoring of PM_{10} only samples the air mass around the ground, while ZJU-HSRL and AERONET products comprehensively consider the information of the whole profile.

3.2.2. Case 2: mega dust storm event, March 15 to 18, 2021

From March 15th to 18th, 2021, a mega dust event occurred. A dust outbreak with a similar magnitude, to the best of our knowledge, had not happened over East Asia in the past 10 years (Liang et al., 2022; Zhang et al., 2023). The dust plume affected >3.8 million square kilometers of East Asia (Gui et al., 2022; He et al., 2022; Liang et al., 2021). The UVAI in Fig. S1 shows that a strong dust plume was observed over Beijing on March 15th with a maximum UVAI of 4.5, and the daily averaged PM_{10} concentration reached 2600 μg/m^3. The distribution of UVAI indicates that most regions in northern China were suffering from this mega dust event. Although several researchers have investigated the dynamic mechanism, transport, and impacts of this dust storm event using in situ observations, reanalysis data, and climate models, the information on its vertical distribution is still inadequate (Liang et al., 2022; Yin et al., 2021; Zhang et al., 2023).

ZJU-HSRL observed the complete diurnal changes of this mega dust storm event at the Tower Branch of the Institute of Atmospheric Physics, as shown in Fig. 5. Compared with case 1, the outbreak of this dust event is stronger, faster, and has a more complicated atmospheric vertical structure. Before the arrival of the dust storm, a water cloud with a high scattering ratio and a very small PLDR was observed 0.5 km above the surface. At 6:00 (UTC + 8) on March 15th, dust aerosols were advected to the observation site, and they settled down to the ground in only 1–2 h. The extinction coefficient observed by ZJU-HSRL is >1 km^{-1}, and the strong aerosol loading makes the laser energy attenuate rapidly, leading to an effective detection range of <1 km. From the evening of March 15th to the afternoon of March 16th, as the dust aerosol settled and dissipated, the extinction

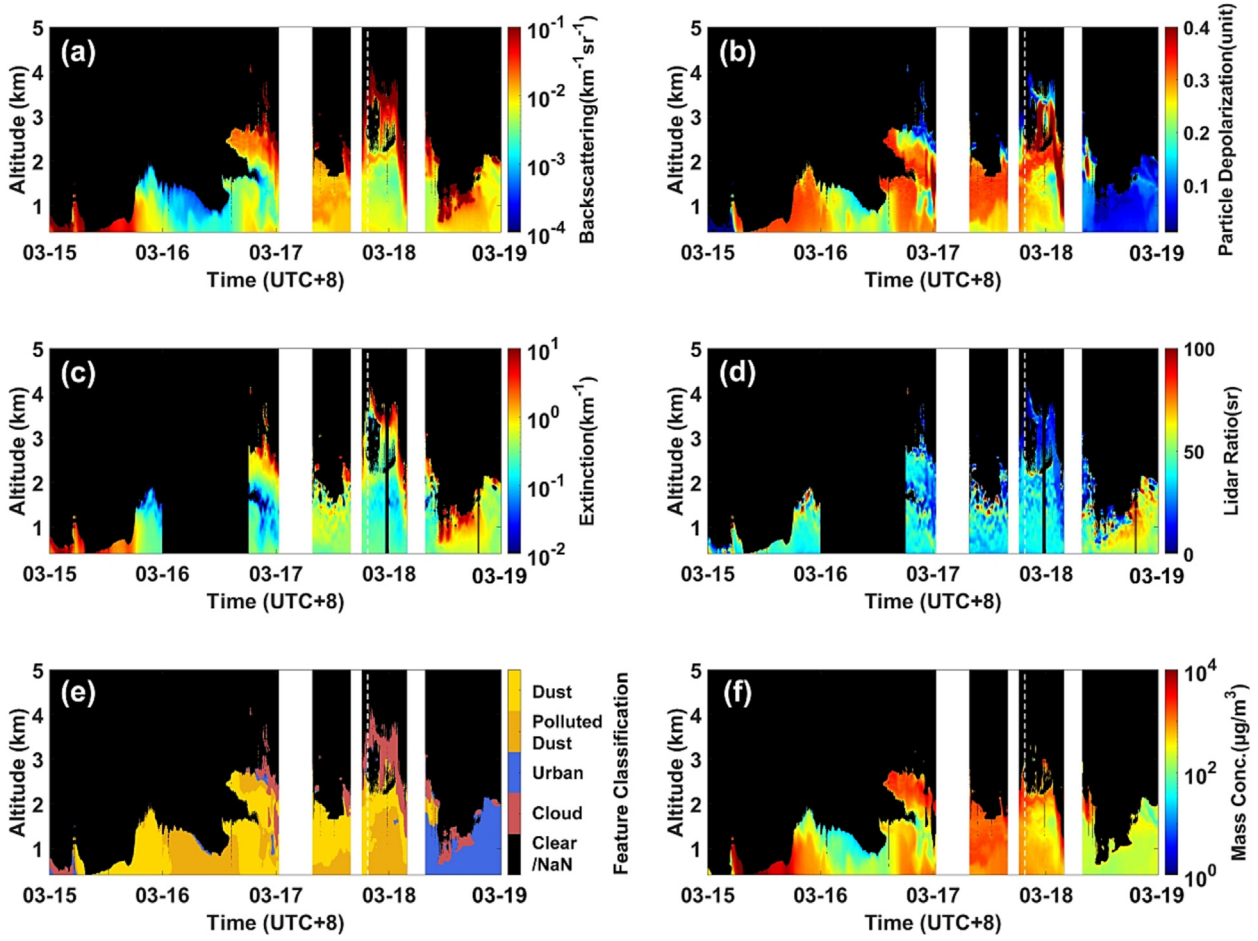

Fig. 5. The same as Fig. 3, but observed from March 15th to 18th, 2021 at the Tower Branch of the Institute of Atmospheric Physics. The areas in white represent the downtime of the system due to rain and system adjustments and the lack of lidar ratio and extinction during part of the observation periods was due to the misalignment of the wide-FOV channel. The dotted white lines are shown in Fig. 6.

coefficient and PLDR decreased, and the boundary layer height measured by HSRL was about 2 km. Two dust plumes were transported to the observation site on the night of March 16th. One plume settled to the surface and the other one appeared at around 2.5 km, as can be seen from Fig. 5 (b)(e)(f). With the mixing of aerosols, the vertical structure transformed into a double-layer structure of polluted dust (bottom) and pure dust (upper) before noontime of the 17th. In addition, ice clouds with large PLDRs were observed at 2–4 km.

The LR and PLDR of dust were 42 ± 5 sr and 0.31 ± 0.01 during the dust event, respectively. The areas in white represented the downtime of the system and the lack of lidar ratio and extinction during part of the observation periods was due to the misalignment of the wide-FOV channel. In that latter case, we could not calculate extinction and LR. The dust event ended on the morning of March 18th, when the LR increased to 55 ± 7 sr while the PLDR decreased to 0.08 ± 0.02. These values are consistent with the characteristics of typical urban aerosols, and the results from feature classification show the presence of urban aerosols and low-level water clouds with low PLDR at the top of the boundary layer.

The aerosol backscattering coefficient, extinction coefficient, PLDR, LR, and mass concentration profile observed by ZJU-HSRL at 12:35 (UTC + 8) on January 11th, 2021, are shown in Fig. 6 (a)-(e). The PLDR below 1 km increased with height and kept stable at 1–2.5 km with a value of 0.31 ± 0.02. The LR is stable over the entire profile, with values ranging from 30 ± 6 to 51 ± 14 sr. These intensive properties indicate that the aerosol type changed from polluted dust below 1.2 km to a pure-dust layer distributed between 1.2 and 2.5 km. The backscattering, extinction as well as dust mass concentration were uniformly distributed within the polluted dust layer, and the center of the dust layer was at 2.2 km height above ground level. The vertically resolved distribution of optical properties and mass concentration helps with a better understanding of the mixing process of dust aerosols with local aerosols.

Fig. 6 (f) shows the backward trajectories at 00:00 (UTC) on March 17th. The transmission paths of trajectories at different heights are slightly different, but all of them arrive from the west side of Beijing. Taklimakan dust and other dust aerosols dominated this dust event, as the UVAI shows in Fig. S1. The backward trajectories well verify the rationality of HSRL results in Fig. 5.

The time series of ZJU-HSRL observations and surface auxiliary data are shown in Fig. 6 (h)-(j). Before 7:00 (UTC + 8) on March 15th, the relative humidity near the surface was 77 % to 94 % and a thick water cloud was detected by ZJU-HSRL at around 0.5 km. The low PLDR (~0.15) indicates the predominance of fine-mode particles. Subsequently, the dust aerosol was transported to the observation site with the strengthened wind. The arrival of dust plumes led to a rapid decrease of relative humidity of below 15 % and a significant increase of surface PM_{10} concentration with a maximum value of 7525 μg/m^3 at 9:00 (UTC + 8). The averaged PLDR observed by ZJU-HSRL rose nearly simultaneously from 0.10 ± 0.09 to 0.29 ± 0.05 within 1–2 h, and the retrieved particle mass concentration increased

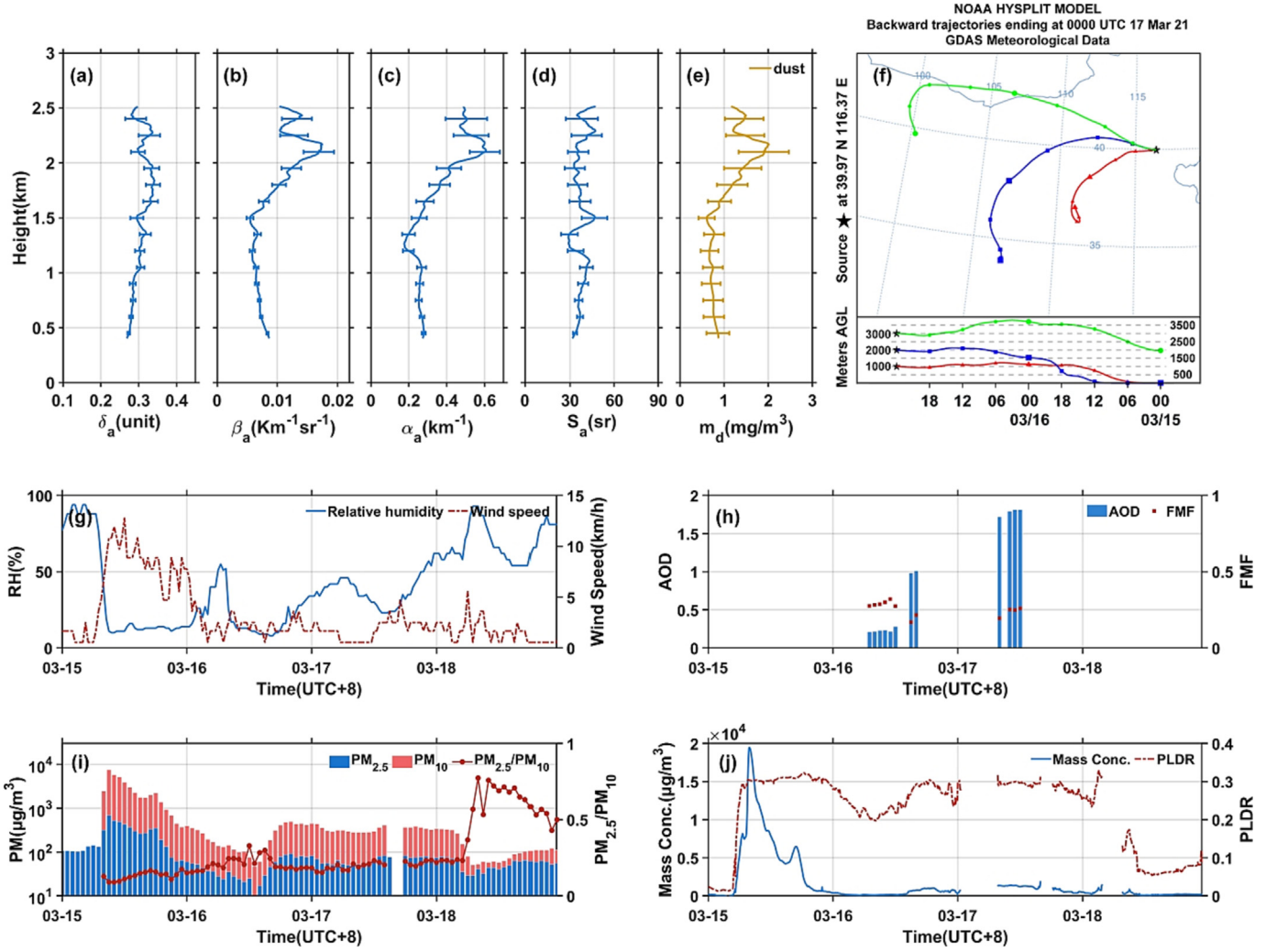

Fig. 6. The same as Fig. 4, but (a)-(e) are observed at 12:35 (UTC + 8) on March 17th, 2021, (f) is the 48 h HYSPLIT backward trajectories at 00:00 (UTC) on March 17th at 1000 m (red), 2000 m (blue), and 3000 m (green) above ground level and (g)-(h) are observed from March 15th to 18th, 2021. The observation location is at the Tower Branch of the Institute of Atmospheric Physics. (For interpretation of the references to colour in this figure legend, the reader is referred to the web version of this article.)

significantly to a maximum of 19,484 ± 356 μg/m^3 at 07:55 (UTC + 8). Both the abnormally large peak values and the rapid change of mass concentration point to the particularity of this dust event. Subsequently, the dust aerosol loading decreased, and surface PM_{10} concentration dropped to a minimum value of 47 μg/m^3 at 13:00 (UTC + 8) on the 16th. Although the particle mass concentration dropped significantly, the high PLDR (>0.2) observed by ZJU-HSRL and low $PM_{2.5}/PM_{10}$ ratio (<0.33) in Fig. 6 (i) indicate that non-spherical coarse mode particles are the main contributor. After 16:00 (UTC + 8) on the 16th, the arrival of the second dust plumes caused the PM_{10} concentration to re-exceed 150 μg/m^3. Also, AOD from AERONET increased from 0.2 to about 1. Although the dust aerosol mass concentration varied widely during the dust event, the $PM_{2.5}/PM_{10}$ ratio and the FMF determined by aerosol microphysical properties remained small and stable. Likewise, PM_{10} concentration lagged behind the detection of the dust plume by ZJU-HSRL and AERONET by 1–6 h. The low PM_{10} concentration, low PLDR, and high $PM_{2.5}/PM_{10}$ ratio after 6:00 (UTC + 8) on March 18th are consistent with the low PLDR and dust mass concentration observed by ZJU-HSRL, which indicate the end of the dust event and the return of urban aerosol as the dominant aerosol type.

3.3. Comparison to auxiliary data

To demonstrate the rationality of our observations, surface PM_{10} concentrations, and AOD products from the sun photometer were used to validate the results. The comparison between the surface PM_{10} concentration and the total particle mass concentration obtained by ZJU-HSRL at 300 m height above ground is shown in Fig. 7 (a). For the sake of comparison, the temporal resolution is unified to 1 h and we obtained 1934 pairs of the hourly averaged mass concentration and surface PM_{10} concentration. We find a satisfactory correlation between the surface PM_{10} concentration and the particle mass concentration retrieved by ZJU-HSRL. The correlation coefficient R = 0.9. Furthermore, we found that the particle mass concentration obtained by ZJU-HSRL is greater than the values obtained from PM_{10} monitoring, which could be attributed to several reasons. (1) The pollution as seen from lidar observations at 300 m is more pronounced than that from PM_{10} monitoring at the surface because dust aerosol is transported from desert areas at high altitudes (Wang et al., 2021b). (2) The different detection ranges of the particle size distribution by different methods, that is, the particle mass concentration retrieved by HSRL is not limited to a particle size of <10 μm while in situ measurements methods have inlet cut-off effect. Usually, large particles have greater mass. (3) The difference in mass density, conversion factor, and particle shape caused by atmospheric relative humidity may be a source of disagreement in the results (Ansmann et al., 2012; Ren et al., 2021; Wang et al., 2022a; Wang et al., 2021b).

Fig. 7 (b) presents the comparison of the AODs retrieved by ZJU-HSRL and the sun photometer, where the red solid line is the fitting line. The comparison uses the interpolated 500 nm AOD, which is one of the standard data products provided by AERONET. We matched HSRL data with AERONET data during the whole observation period, and a total of 7578 point-to-point data was obtained. The comparison results show that the slope of the fitted line is 0.98, the bias is 0.05, and the correlation coefficient R = 0.94, indicating the AODs obtained by the two instruments show good agreement.

3.4. Comparison to historical observations

Fig. 8 presents the comparison of (a) lidar ratio and (b) particle linear depolarization ratio of Asian dust measured with ZJU-HSRL and reported for previous RL observations. The error bars represent the standard deviations and the results without error bars are because the standard deviations are not provided in previous publications. Detailed values are listed in Table S3 in SI. Despite the dataset of dust aerosols being crucial to climate and environment research, studies of their intensive properties such as LR and PLDR are still scarce and sparsely distributed, especially in East Asia. The LR values of dust aerosols in Beijing are 38 ± 7 sr (Tesche et al., 2007) and 38 ± 10 sr (Xie et al., 2008), respectively, which are in good agreement with our results. However, these observations did not simultaneously provide dust aerosol PLDR. Our observations show that the PLDR of dust over Beijing is 0.31 ± 0.02 at 532 nm. Observations in other downwind regions show that LR and PLDR are 35 to 47 sr and 0.29 to 0.37, respectively (Filioglou et al., 2020; Murayama et al., 2004; Tatarov et al., 2012). The results are close to what we found but still show some differences, which may be attributed to the different transport paths and mixture state of the dust plume. The PLDR of a dust plume observed over Tokyo, Japan is ~0.2, which is much smaller than that at other observation sites (Murayama et al., 2004). A possible explication is that dust aerosols were mixed with local aerosols. The LR and PLDR of the Taklimakan dust observed in Kashi, China are 45 ± 7 sr and 0.36 ± 0.05, respectively, which are larger than those observed in downwind areas (Hu et al., 2020). The difference in LR and PLDR of the dust source region and downwind areas may be attributed to the difference in size, mixing, and aging of the mineral dust (Groß et al., 2015; Mona et al., 2012). Also, the abundance of big dust particles in the source region may strongly increase the PLDR compared to downwind areas (Hu et al., 2020). We found that the PLDR of Asian dust is similar to that of American dust and Saharan dust as shown in Table S4 in SI, but Asian dust LR is much smaller, which may be attributed to the difference in microphysical properties of different dust sources. Furthermore, we discovered that almost all previous studies of Asian dust properties came from RL observations, and to the best of our knowledge, this is the first report of HSRL observation of dust aerosol in China. With a higher signal-to-noise ratio (compared to RL), HSRL can track and observe dust events throughout the day, which helps to further improve and expand the dust aerosol database and provides important support for further understanding the evolution of dust events.

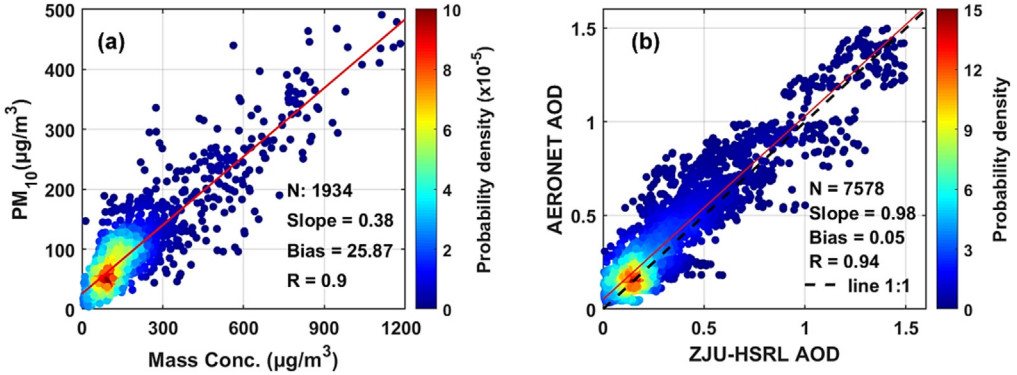

Fig. 7. (a) Comparison between mass concentration detected by ZJU-HSRL at 300 m and surface PM_{10} concentration. (b) Comparison of AODs retrieved by ZJU-HSRL and sun photometer (500 nm). The red line is the fitting line. (For interpretation of the references to colour in this figure legend, the reader is referred to the web version of this article.)

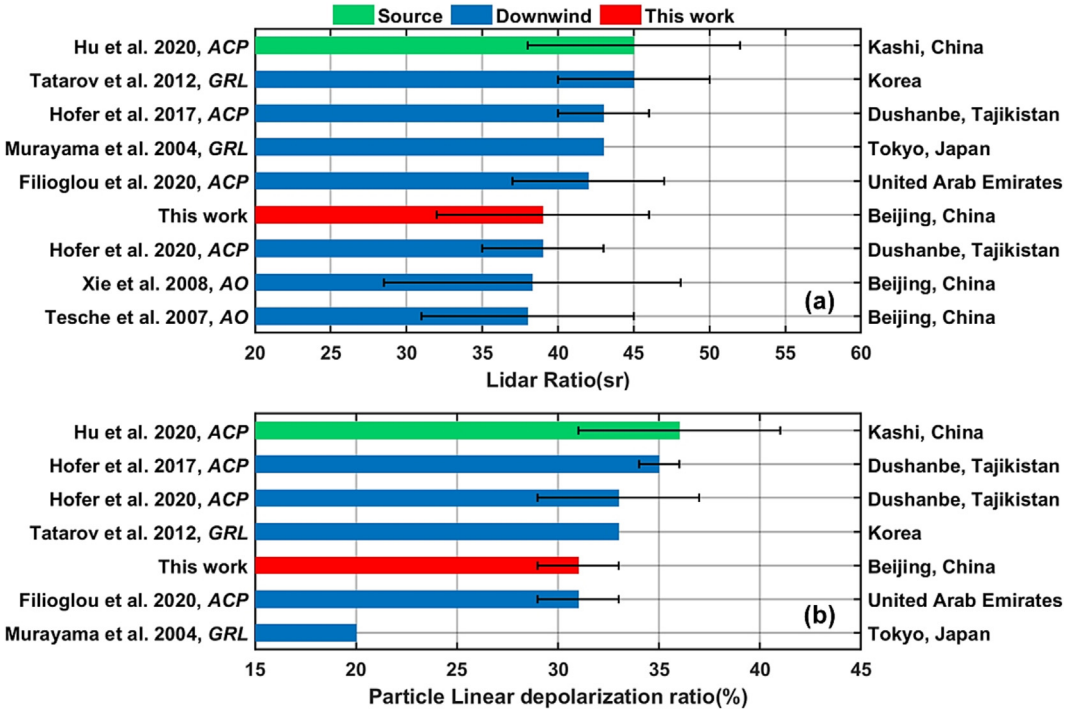

Fig. 8. Comparison of (a) lidar ratio and (b) particle linear depolarization ratio of Asian dust. Data were obtained from ZJU-HSRL and previous RL observations. The error bars represent the standard deviations. The results without error bars are because the standard deviations are not provided in previous publications. The specific values are listed in Table S3 in SI.

3.5. The relationship between the PLDR and dust proportion

The intensive property PLDR, values of which are determined by the aerosol type, is widely used to characterize dust aerosol properties. PDLR however does not allow for inferring dust aerosol loading and thus limits our understanding of dust events. Dust AOD and dust mass concentration could be used for an interpretation of dust events intensity to a certain extent, but they fluctuate significantly during the dust events. Dust aerosols are usually mixed with other aerosols, especially in downwind areas. Quantifying the contribution of dust aerosols is essential to improve the understanding of the impact of dust aerosols on climate and the environment. It would undoubtedly improve our understanding of the contribution of dust if a simple and effective method is developed to assess dust mass concentration proportion along with dust optical properties proportion.

The variations of mean dust mass concentration proportion (orange points), mean dust backscattering proportion (blue points), and dust AOD proportion (red points) with the mean PLDR observed by ZJU-HSRL from November 2021 to March 2022 are presented in Fig. 9. The variation tendencies of these observations suggest that the PLDR has the potential to directly assess the dust mass concentration proportion, AOD proportion, and backscattering proportion if the corresponding fitted regression equations are determined.

We try to explain this phenomenon from a mathematical point of view. It is easily found from the Eq. (3) that the dust backscattering proportion ($\frac{\beta_d}{\beta_d+\beta_{nd}}$) is a function of PLDR (Shin et al., 2014). The dust backscattering proportion can be uniquely determined by PLDR after selecting the parameters in the POLIPHON method. By combining Eqs. (2), (4)–(5), we find that both the dust extinction ($\frac{\alpha_d}{\alpha_d+\alpha_{nd}}$) and the mass concentration proportion ($\frac{m_d}{m_d+m_{nd}}$) can be expressed as functions of PLDR. These expressions are similar to the function of the dust backscattering proportion. The detailed information on the analytical relationships is summarized in Table 1. We find that the analytical relationship of dust mass concentration proportion is in good agreement with the ZJU-HSRL observations with $R = 0.96$, as the orange line shown in Fig. 9. The blue line in Fig. 9 represents the analytical relationship of dust backscattering proportion with PLDR. It also agrees well with the mean dust backscattering proportion observed by ZJU-HSRL with the correlation coefficient $R = 0.99$. Furthermore, we studied the analytical relationship between PLDR and dust AOD proportion ($\frac{\tau_d}{\tau_d+\tau_{nd}}$). Our analysis indicates that when the mean PLDR is used as a constant instead of PLDR, the dust AOD proportion can be solved by the analytical expression in the same fashion as the dust extinction proportion. The analytic equation, as the red line portrayed in Fig. 9, performs well in the ZJU-

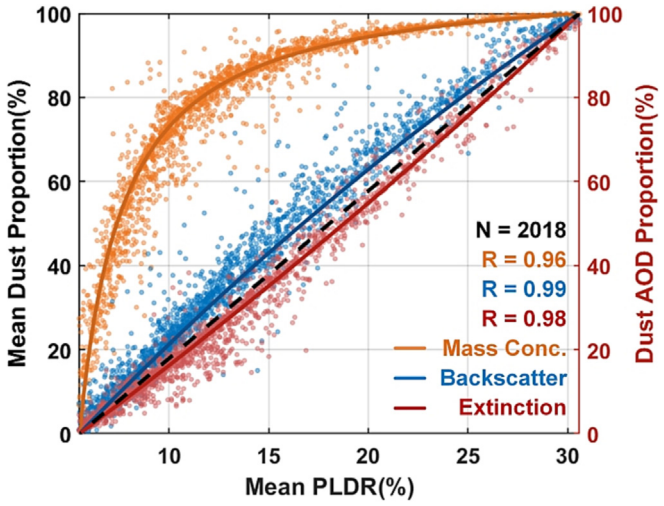

Fig. 9. The variations of mean dust mass concentration proportion (orange points), mean dust backscattering proportion (blue points), and dust AOD proportion (red points) with the mean PLDR observed by ZJU-HSRL from November 2021 to March 2022. The orange, blue and red lines represent the relationship between dust mass concentration proportion, dust backscattering proportion, and dust extinction proportion, respectively, with PLDR. The specific relationships of analytical relationships are summarized in Table 1. (For interpretation of the references to colour in this figure legend, the reader is referred to the web version of this article.)

Table 1
Universal analytical relationship between PLDR and dust proportion.

Universal analytical relationship $f(\delta_a) = \frac{1}{C_1}\left(1 - \frac{C_2}{C_3\delta_a + C_4}\right)$				
$f(\delta_a)$	C_1	C_2	C_3	C_4
$\frac{\beta_d}{\beta_d+\beta_{nd}}$	$\frac{\delta_d - \delta_{nd}}{1+\delta_d}$	$\delta_{nd} + 1$	1	1
$\frac{\alpha_d}{\alpha_d+\alpha_{nd}}$	$1 + \frac{S_{nd}}{S_d}\left(\frac{\delta_d - \delta_{nd}}{1+\delta_d} - 1\right)$	$\frac{S_{nd}}{S_d}\frac{\delta_d - \delta_{nd}}{1+\delta_d}(1+\delta_{nd})$	C_1	$C_2 - C_1\delta_{nd}$
$\frac{\tau_d}{\tau_d+\tau_{nd}}$	$1 + \frac{S_{nd}}{S_d}\left(\frac{\delta_d - \delta_{nd}}{1+\delta_d} - 1\right)$	$\frac{S_{nd}}{S_d}\frac{\delta_d - \delta_{nd}}{1+\delta_d}(1+\delta_{nd})$	C_1	$C_2 - C_1\delta_{nd}$
$\frac{m_d}{m_d+m_{nd}}$	$1 + \frac{\rho_{nd}\overline{\nu_f/\tau_f}}{\rho_d\nu_c/\tau_c}\frac{S_{nd}}{S_d}\left(\frac{\delta_d - \delta_{nd}}{1+\delta_d} - 1\right)$	$\frac{\rho_{nd}\overline{\nu_f/\tau_f}}{\rho_d\nu_c/\tau_c}\frac{S_{nd}}{S_d}\frac{\delta_d - \delta_{nd}}{1+\delta_d}(1+\delta_{nd})$	C_1	$C_2 - C_1\delta_{nd}$

HSRL data with $R = 0.98$. These findings also verify the reliability and accuracy of ZJU-HSRL observation results.

The derived analytical relationships are verified by extracting observation results from previous studies. The observations of dust and smoke aerosols over Cape Verde (Tesche et al., 2009) showed that the dust backscattering proportion increased from ~30 % to over 95 % when PLDR varied from ~0.12 to ~0.31 and the dust extinction proportion rose from ~20 % to ~75 % (PLDR is ~0.24). Substituting these observations into our deduced analytical relationship, the results are in good agreement, which demonstrates the correctness of the universal analytical equation. The dust mass concentration proportion was >80 % when PLDR is about 0.15 (Hofer et al., 2020; Wang et al., 2021b). Although it is slightly smaller than the result we obtain from our analytical equation, it is understandable and acceptable given the difference in input parameters of the POLIPHON method and the uncertainty of retrieved optical properties.

Thus, inspired by the observations from ZJU-HSRL, we found a universal analytical relationship to directly evaluate the contribution of dust aerosol by PLDR. Benefitting from this universal functional analytical relationship, we can directly evaluate the proportion of dust mass concentration, backscattering, extinction, and AOD using PLDR. This interesting finding is expected to expand the application of polarization technology in dust detection and provides a simple and effective method for quantifying dust aerosol contribution.

4. Conclusions

Dust aerosols, as an important component of atmospheric aerosols, significantly impact climate, environment, and human health. Dust aerosols from arid desert areas are transported over long distances and affect the environment and air quality in downwind areas. To the best of our knowledge, it is the first time that HSRL observations were carried out to investigate dust aerosols' mass concentration and optical properties. In particular, we calculated the mass concentration, backscattering coefficients, extinction coefficients, LR, and PLDR of dust plumes. The first three properties contribute to a better understanding of the intensity of dust loading during the dust events while the latter two are intensive lidar properties that depend on aerosol type regardless of dust concentration. It is found from AERONET observations that Beijing was severely affected by dust aerosols, especially in March, in which the monthly averaged AOD reached 0.94, and the percentage of observation days with AE <0.5 accounted for 38.1 % (8/21). Two dust events are presented, including a case of dust aerosol intrusion into the boundary layer and a case of a mega dust storm event. Compared with previous RL observation, HSRL possesses a superior signal-to-noise ratio and thus can observe the diurnal changes of the dust transport process, and thus provide more comprehensive and detailed observational information for studying the evolution of dust aerosol properties and understanding mixing processes of aerosols.

Dust aerosols first appeared at the top of the boundary layer, and then gradually affected the vicinity of the surface. The sedimentation time varies with the intensity of the dust event, and the fastest sedimentation can be 1–2 h such as in Case 2. Thus, the vertical structure of aerosols during these two dust events is usually displayed as a bilayer structure, i.e. an upper layer of dust aerosol and a lower layer of polluted dust resulting from the mixing with urban aerosols. The spatiotemporal evolution of dust aerosol loading during the dust event is particularly complicated. The dust aerosol loading may vary between the maximum and minimum concentrations and last for several days due to the persistent replenishment of dust aerosols. The particle mass concentrations retrieved by ZJU-HSRL vary greatly during these two dust events, with the maximum reaching $(1.52 \pm 0.35)\ x10^3\ \mu g/m^3$ and $(19.48 \pm 0.36)\ x10^3\ \mu g/m^3$ for the two cases, respectively. However, the values of the intensive properties are relatively invariable. The 532 nm PLDR and LR of the transported dust aerosols are 0.31 ± 0.02 and 39 ± 7 sr, respectively. As for urban, the 532 nm PLDR and LR are 0.08 ± 0.02 and 55 ± 7 sr, respectively. These valuable databases can provide a reference for climate models and reduce the uncertainties of model predictions.

To verify the ZJU-HSRL results, we compare the ZJU-HSRL observations with surface PM_{10} concentrations and AOD from the sun photometer. The particle mass concentration retrieved by ZJU-HSRL has a satisfactory consistency with surface PM_{10} concentration and the correlation coefficient $R = 0.9$. The results show that the AOD observed by ZJU-HSRL and the sun photometer are in good agreement, with a correlation coefficient of $R = 0.95$. We compare the PLDRs and LRs of dust aerosols with historical Raman lidar observations. The observed PLDRs and LRs are lower compared to those obtained in the dust source region, which may be due to the influence of large dust particles near the source region and the aging effects of dust particles. Compared with the observations from other downwind sites, the values of LR and PLDR are generally close.

By analyzing the observations of ZJU-HSRL, we found that the PLDR has the potential to directly assess the contribution of dust aerosols. A universal analytical relationship to evaluate the proportion of dust aerosol backscattering, extinction, and mass concentration by PLDR is discovered. The measured mean dust backscattering proportion and dust mass concentration proportion have a good correlation ($R \geq 0.96$) with the corresponding analytical equations. The universal analytical equation also works well for characterizing the relationship between dust AOD proportion and mean PLDR, which is verified by the observations with $R = 0.98$. These comparisons with high consistency also reflect the reliability of the observation from ZJU-HSRL from another perspective. Moreover, the comparison of the results from the observations in previous studies with the results of the analytical relationship is in good agreement, which verifies the correctness of the derived analytical equation. Hence, we can directly evaluate the proportion of dust mass concentration, backscattering, extinction and AOD by PLDR. This analytical relationship is expected to expand the application of polarization technology in dust detection and provides a simple and effective method for quantifying dust aerosol contribution. These valuable observations could contribute to further understanding the contribution of dust aerosol to the environment and climate and help in supplementing the dust aerosol database, which was lacking in previous studies and climate model studies.

CRediT authorship contribution statement

Da Xiao: Conceptualization, methodology, formal analysis, writing – original draft preparation, review & editing; Nanchao Wang: Methodology, formal analysis, data curation, writing – original draft preparation; Sijie Chen: Data curation, writing – review & editing; Lingyun Wu: Resources; Detlef Müller: Formal analysis, writing – review & editing; Igor Veselovskii:

Writing – review & editing; Chengcai Li: Writing – review & editing; Eduardo Landulfo: Writing – review & editing; Venkataraman Sivakumar: Writing – review & editing; Jing Li: Writing – review & editing; Huizheng Che: Writing – review & editing; Jing Fang: Visualization; Kai Zhang: Data curation; Binyu Wang: Resources; Feitong Chen: Resources; Xianzhe Hu: Data curation; Xiaotao Li: Visualization; Weize Li: Formal analysis; Yicheng Tong: Data curation; Ju Ke: Data curation; Lan Wu: Writing – review & editing; Chong Liu: Supervision; Dong Liu: Conceptualization, formal analysis, writing – review & editing, funding acquisition.

Data availability

Data will be made available on request.

Declaration of competing interest

The authors declare that they have no known competing financial interests or personal relationships that could have appeared to influence the work reported in this paper.

Acknowledgments

This work was supported by the Excellent Young Scientist Program of Zhejiang Provincial Natural Science Foundation of China (LR19D050001); National Key Research and Development Program of China (2016YFC0200700); Fundamental Research Funds for the Central Universities (2021XZZX019); State Key Laboratory of Modern Optical Instrumentation Innovation Program (MOI2020ZD02); Zhejiang University Global Partnership Fund, and Russian Science Foundation (project 21-17-00114).

The authors acknowledge the National Oceanic and Atmospheric Administration (NOAA) Air Resources Laboratory (ARL) for the provision of the HYSPLIT transport and dispersion model used in this publication. Concerning the AERONET data used in this paper, we thank the Chinese Academy of Meteorological Sciences for establishing and maintaining the Beijing_CAMS site. We'd like to sincerely thank NASA's Ozone Product Evaluation and Test Element (PEATE) team for the provision of Ultraviolet Aerosol Index data (https://ozoneaq.gsfc.nasa.gov/omps/). We would like to thank the Beijing Municipal Ecological and Environmental Monitoring Center for the provision of the PM concentration data (http://www.bjmemc.com.cn/). We also gratefully acknowledge the ECMWF for the provision of the ERA5 dataset.

Appendix A. Supplementary data

Supplementary data to this article can be found online at https://doi.org/10.1016/j.scitotenv.2023.162091.

References

Adebiyi, A.A., Kok, J.F., 2020. Climate models miss most of the coarse dust in the atmosphere. <sb:contribution><sb:title>Sci. </sb:title></sb:contribution><sb:host><sb:issue><sb:series><sb:title>Adv.</sb:title></sb:series></sb:issue></sb:host> 6, eaaz9507. https://doi.org/10.1126/sciadv.aaz9507.

Ansmann, A., Seifert, P., Tesche, M., Wandinger, U., 2012. Profiling of fine and coarse particle mass: case studies of Saharan dust and Eyjafjallajökull/Grimsvötn volcanic plumes. Atmos. Chem. Phys. 12, 9399–9415. https://doi.org/10.5194/acp-12-9399-2012.

Ansmann, A., Mamouri, R.E., Hofer, J., Baars, H., Althausen, D., Abdullaev, S.F., 2019. Dust mass, cloud condensation nuclei, and ice-nucleating particle profiling with polarization lidar: updated POLIPHON conversion factors from global AERONET analysis. Atmos. Meas.Techn. 12, 4849–4865. https://doi.org/10.5194/amt-12-4849-2019.

Binietoglou, I., Basart, S., Alados-Arboledas, L., Amiridis, V., Argyrouli, A., Baars, H., Baldasano, J.M., Balis, D., Belegante, L., Bravo-Aranda, J.A., Burlizzi, P., Carrasco, V., Chaikovsky, A., Comerón, A., D'Amico, G., Filioglou, M., Granados-Muñoz, M.J., Guerrero-Rascado, J.L., Ilic, L., Kokkalis, P., Maurizi, A., Mona, L., Monti, F., Muñoz-Porcar, C., Nicolae, D., Papayannis, A., Pappalardo, G., Pejanovic, G., Pereira, S.N., Perrone, M.R., Pietruczuk, A., Posyniak, M., Rocadenbosch, F., Rodríguez-Gómez, A., Sicard, M., Siomos, N., Szkop, A., Terradellas, E., Tsekeri, A., Vukovic, A., Wandinger, U., Wagner, J., 2015. A methodology for investigating dust model performance using synergistic EARLINET/AERONET dust concentration retrievals. Atmos.Meas.Techn. 8, 3577–3600. https://doi.org/10.5194/amt-8-3577-2015.

Bohlmann, S., Baars, H., Radenz, M., Engelmann, R., Macke, A., 2018. Ship-borne aerosol profiling with lidar over the Atlantic Ocean: from pure marine conditions to complex dust–smoke mixtures. Atmos. Chem. Phys. 18, 9661–9679. https://doi.org/10.5194/acp-18-9661-2018.

Bravo-Aranda, J., Titos, G., José, M., Oz, G.-M., Lui, J., Guerrero-Rascado, S., Guzmán, F., Gutiérrez, A., Lyamani, H., Olmo, F., Andrey, J., Arboledas, L., 2015. Study of mineral dust entrainment in the planetary boundary layer by lidar depolarisation technique. Tellus Ser. B Chem. Phys. Meteorol. 67, 26180. https://doi.org/10.3402/tellusb.v67.26180.

Burton, S.P., Ferrare, R.A., Hostetler, C.A., Hair, J.W., Rogers, R.R., Obland, M.D., Butler, C.F., Cook, A.L., Harper, D.B., Froyd, K.D., 2012. Aerosol classification using airborne high spectral resolution lidar measurements – methodology and examples. Atmos.Meas. Techn. 5, 73–98. https://doi.org/10.5194/amt-5-73-2012.

Cao, C., Zheng, S., Singh, R.P., 2014. Characteristics of aerosol optical properties and meteorological parameters during three major dust events (2005–2010) over Beijing, China. Atmos. Res. 150, 129–142. https://doi.org/10.1016/j.atmosres.2014.07.022.

Che, H., Gui, K., Xia, X., Wang, Y., Holben, B.N., Goloub, P., Cuevas-Agulló, E., Wang, H., Zheng, Y., Zhao, H., Zhang, X., 2019. Large contribution of meteorological factors to inter-decadal changes in regional aerosol optical depth. Atmos. Chem. Phys. 19, 10497–10523. https://doi.org/10.5194/acp-19-10497-2019.

Chen, S., Tong, B., Russell, L.M., Wei, J., Guo, J., Mao, F., Liu, D., Huang, Z., Xie, Y., Qi, B., Zhang, H., Sun, Y., Zhang, B., Xu, C., Wu, L., Liu, D., 2022. Lidar-based daytime boundary layer height variation and impact on the regional satellite-based PM2.5 estimate. Remote Sens. Environ. 281, 113224. https://doi.org/10.1016/j.rse.2022.113224.

Cheng, Z., Liu, D., Luo, J., Yang, Y., Su, L., Yang, L., Huang, H., Shen, Y., 2014. Effects of spectral discrimination in high-spectral-resolution lidar on the retrieval errors for atmospheric aerosol optical properties. Appl. Opt. 53, 4386–4397. https://doi.org/10.1364/AO.53.004386.

Creamean, J.M., Suski, K.J., Rosenfeld, D., Cazorla, A., DeMott, P.J., Sullivan, R.C., White, A.B., Ralph, F.M., Minnis, P., Comstock, J.M., Tomlinson, J.M., Prather, K.A., 2013. Dust and biological aerosols from the Sahara and Asia influence precipitation in the Western U.S. Science 339, 1572–1578. https://doi.org/10.1126/science.1227279.

Dubovik, O., Holben, B., Eck, T., Smirnov, A., Kaufman, Y., King, M., Tanré, D., Slutsker, I., 2002. Variability of absorption and optical properties of key aerosol types observed in worldwide locations. J. Atmos. Sci. 59, 590–608. https://doi.org/10.1175/1520-0469(2002)059<0590:VOAAOP>2.0.CO;2.

Engelmann, R., Kanitz, T., Baars, H., Heese, B., Althausen, D., Skupin, A., Wandinger, U., Komppula, M., Stachlewska, I.S., Amiridis, V., Marinou, E., Mattis, I., Linné, H., Ansmann, A., 2016. The automated multiwavelength Raman polarization and water-vapor lidar PollyXT: the neXT generation. Atmos.Meas.Techn. 9, 1767–1784. https://doi.org/10.5194/amt-9-1767-2016.

Filioglou, M., Giannakaki, E., Backman, J., Kesti, J., Hirsikko, A., Engelmann, R., O'Connor, E., Leskinen, J.T.T., Shang, X., Korhonen, H., Lihavainen, H., Romakkaniemi, S., Komppula, M., 2020. Optical and geometrical aerosol particle properties over the United Arab Emirates. Atmos. Chem. Phys. 20, 8909–8922. https://doi.org/10.5194/acp-20-8909-2020.

Freudenthaler, V., Esselborn, M., Wiegner, M., Heese, B., Tesche, M., Ansmann, A., Muller, D., Althausen, D., Wirth, M., Fix, A., Ehret, G., Knippertz, P., Toledano, C., Gasteiger, J., Garhammer, M., Seefeldner, M., 2009. Depolarization ratio profiling at several wavelengths in pure Saharan dust during SAMUM 2006. Tellus Ser. B Chem. Phys. Meteorol. 61, 165–179. https://doi.org/10.1111/j.1600-0889.2008.00396.x.

Gandham, H., Dasari, H.P., Karumuri, A., Ravuri, P.M.K., Hoteit, I., 2022. Three-dimensional structure and transport pathways of dust aerosols over West Asia. <sb:contribution><sb:title>npj Clim. Atmos.</sb:title></sb:contribution><sb:host><sb:issue><sb:series><sb:title>Sci.</sb:title></sb:series></sb:issue></sb:host> 5, 45. https://doi.org/10.1038/s41612-022-00266-2.

Groß, S., Esselborn, M., Weinzierl, B., Wirth, M., Petzold, A.J.A.C., 2013. Aerosol classification by airborne high spectral resolution lidar observations. Atmos. Chem. Phys. 12, 25983–26028. https://doi.org/10.5194/acp-13-2487-2013.

Groß, S., Freudenthaler, V., Schepanski, K., Toledano, C., Schäfler, A., Ansmann, A., Weinzierl, B., 2015. Optical properties of long-range transported Saharan dust over Barbados as measured by dual-wavelength depolarization Raman lidar measurements. Atmos. Chem. Phys. 15, 11067–11080. https://doi.org/10.5194/acp-15-11067-2015.

Gui, K., Yao, W., Che, H., An, L., Zheng, Y., Li, L., Zhao, H., Zhang, L., Zhong, J., Wang, Y., Zhang, X., 2022. Record-breaking dust loading during two mega dust storm events over northern China in march 2021: aerosol optical and radiative properties and meteorological drivers. Atmos. Chem. Phys. 22, 7905–7932. https://doi.org/10.5194/acp-22-7905-2022.

Hair, J.W., Hostetler, C.A., Cook, A.L., Harper, D.B., Ferrare, R.A., Mack, T.L., Welch, W., Izquierdo, L.R., Hovis, F.E., 2008. Airborne high spectral resolution lidar for profiling aerosol optical properties. Appl. Opt. 47, 6734–6752. https://doi.org/10.1364/AO.47.006734.

He, Y., Yi, F., Yin, Z., Liu, F., Yi, Y., Zhou, J., 2022. Mega Asian dust event over China on 27–31 March 2021 observed with space-borne instruments and ground-based polarization lidar. Atmos. Environ. 285, 119238. https://doi.org/10.1016/j.atmosenv.2022.119238.

Hofer, J., Althausen, D., Abdullaev, S.F., Makhmudov, A.N., Nazarov, B.I., Schettler, G., Engelmann, R., Baars, H., Fomba, K.W., Müller, K., Heinold, B., Kandler, K., Ansmann, A., 2017. Long-term profiling of mineral dust and pollution aerosol with multiwavelength polarization Raman lidar at the Central Asian site of Dushanbe, Tajikistan: case studies. Atmos. Chem. Phys. 17, 14559–14577. https://doi.org/10.5194/acp-17-14559-2017.

Hofer, J., Ansmann, A., Althausen, D., Engelmann, R., Baars, H., Abdullaev, S.F., Makhmudov, A.N., 2020. Long-term profiling of aerosol light extinction, particle mass, cloud condensation nuclei, and ice-nucleating particle concentration over Dushanbe, Tajikistan, in Central Asia. Atmos. Chem. Phys. 20, 4695–4711. https://doi.org/10.5194/acp-20-4695-2020.

Holben, B.N., Eck, T.F., Slutsker, I., Tanré, D., Buis, J.P., Setzer, A., Vermote, E., Reagan, J.A., Kaufman, Y.J., Nakajima, T., Lavenu, F., Jankowiak, I., Smirnov, A., 1998. AERONET—a federated instrument network and data archive for aerosol characterization. Remote Sens. Environ. 66, 1–16. https://doi.org/10.1016/S0034-4257(98)00031-5.

Hu, Q., Wang, H., Goloub, P., Li, Z., Veselovskii, I., Podvin, T., Li, K., Korenskiy, M., 2020. The characterization of Taklamakan dust properties using a multiwavelength Raman polarization lidar in Kashi, China. Atmos. Chem. Phys. 20, 13817–13834. https://doi.org/10.5194/acp-20-13817-2020.

IPCC, 2013. Climate Change 2013 – The Physical Science Basis: Working Group I Contribution to the Fifth Assessment Report of the Intergovernmental Panel on Climate Change. Cambridge University Press, Cambridge, United Kingdom and New York, NY, USA https://doi.org/10.1017/CBO9781107415324.

IPCC, 2021. Climate Change 2021: The Physical Science Basis. Contribution of Working Group I to the Sixth Assessment Report of the Intergovernmental Panel on Climate Change. Cambridge University Press, Cambridge, United Kingdom and New York, NY, USA https://doi.org/10.1017/9781009157896.

Jia, L., Zheng, W., Huang, F., 2020. Vacuum-ultraviolet photodetectors. PhotoniX 1, 22. https://doi.org/10.1186/s43074-020-00022-w.

Jiang, B., Zhu, S., Ren, L.H., Shi, L., Zhang, X.L., 2022. Simultaneous ultraviolet, visible, and near-infrared continuous-wave lasing in a rare-earth-doped microcavity. Adv.Photon. 4, 046003. https://doi.org/10.1117/1.Ap.4.4.046003.

Jickells, T.D., An, Z.S., Andersen, K.K., Baker, A.R., Bergametti, G., Brooks, N., Cao, J.J., Boyd, P.W., Duce, R.A., Hunter, K.A., Kawahata, H., Kubilay, N., laRoche, J., Liss, P.S., Mahowald, N., Prospero, J.M., Ridgwell, A.J., Tegen, I., Torres, R., 2005. Global iron connections between desert dust, ocean biogeochemistry, and climate. Science 308, 67–71. https://doi.org/10.1126/science.1105959.

Ke, J., Sun, Y., Dong, C., Zhang, X., Wang, Z., Lyu, L., Zhu, W., Ansmann, A., Su, L., Bu, L., Xiao, D., Wang, S., Chen, S., Liu, J., Chen, W., Liu, D., 2022. Development of China's first space-borne aerosol-cloud high-spectral-resolution lidar: retrieval algorithm and airborne demonstration. PhotoniX 3, 17. https://doi.org/10.1186/s43074-022-00063-3.

Kim, M.H., Omar, A.H., Tackett, J.L., Vaughan, M.A., Winker, D.M., Trepte, C.R., Hu, Y., Liu, Z., Poole, L.R., Pitts, M.C., Kar, J., Magill, B.E., 2018. The CALIPSO version 4 automated aerosol classification and lidar ratio selection algorithm. Atmos.Meas.Techn. 11, 6107–6135. https://doi.org/10.5194/amt-11-6107-2018.

Li, Y., Zheng, W., Huang, F., 2020. All-silicon photovoltaic detectors with deep ultraviolet selectivity. PhotoniX 1, 15. https://doi.org/10.1186/s43074-020-00014-w.

Liang, P., Chen, B., Yang, X., Liu, Q., Li, A., Mackenzie, L., Zhang, D., 2021. Revealing the dust transport processes of the 2021 mega dust storm event in northern China. Sci.Bull. 67, 21–24. https://doi.org/10.1016/j.scib.2021.08.014.

Liang, L., Han, Z., Li, J., Xia, X., Sun, Y., Liao, H., Liu, R., Liang, M., Gao, Y., Zhang, R., 2022. Emission, transport, deposition, chemical and radiative impacts of mineral dust during severe dust storm periods in March 2021 over East Asia. Sci. Total Environ. 852, 158459. https://doi.org/10.1016/j.scitotenv.2022.158459.

Liu, D., Zheng, Z., Chen, W., Wang, Z., Li, W., Ke, J., Zhang, Y., Chen, S., Cheng, C., Wang, S., 2019. Performance estimation of space-borne high-spectral-resolution lidar for cloud and aerosol optical properties at 532 nm. Opt. Express 27, A481–A494. https://doi.org/10.1364/OE.27.00A481.

Lv, L., Xiang, Y., Zhang, T., Chai, W., Liu, W., 2020. Comprehensive study of regional haze in the North China Plain with synergistic measurement from multiple mobile vehicle-based lidars and a lidar network. Sci. Total Environ. 721, 137773. https://doi.org/10.1016/j.scitotenv.2020.137773.

Mamali, D., Marinou, E., Sciare, J., Pikridas, M., Kokkalis, P., Kottas, M., Binietoglou, I., Tsekeri, A., Keleshis, C., Engelmann, R., Baars, H., Ansmann, A., Amiridis, V., Russchenberg, H., Biskos, G., 2018. Vertical profiles of aerosol mass concentration derived by unmanned airborne in situ and remote sensing instruments during dust events. Atmos.Meas.Tech. 11, 2897–2910. https://doi.org/10.5194/amt-11-2897-2018.

Mona, L., Liu, Z., Muller, D., Omar, A., Papayannis, A., Pappalardo, G., Sugimoto, N., Vaughan, M., 2012. Lidar measurements for desert dust characterization: an overview. Adv. Meteorol. 2012, 326265. https://doi.org/10.1155/2012/356265.

Murayama, T., Müller, D., Wada, K., Shimizu, A., Sekiguchi, M., Tsukamoto, T., 2004. Characterization of Asian dust and Siberian smoke with multi-wavelength Raman lidar over Tokyo, Japan in spring 2003. Geophys. Res. Lett. 31, L23103. https://doi.org/10.1029/2004GL021105.

Omar, A.H., Winker, D.M., Vaughan, M.A., Hu, Y., Trepte, C.R., Ferrare, R.A., Lee, K.-P., Hostetler, C.A., Kittaka, C., Rogers, R.R., Kuehn, R.E., Liu, Z., 2009. The CALIPSO automated aerosol classification and lidar ratio selection algorithm. J. Atmos. Ocean. Technol. 26, 1994–2014. https://doi.org/10.1175/2009JTECHA1231.1.

Ren, J., Tan, W., Tian, X., Wu, Z., Li, C., Li, J., Zhao, C., Liu, D., Kang, L., Zhu, T., 2021. Retrieval of aerosol liquid water content from high spectral resolution lidar. Sci. Total Environ. 799, 149423. https://doi.org/10.1016/j.scitotenv.2021.149423.

Shen, X., Wang, N., Veselovskii, I., Xiao, D., Zhong, T., Liu, C., Zhang, K., Zhou, Y., Liu, D., 2020. Development of ZJU high-spectral-resolution lidar for aerosol and cloud: calibration of overlap function. J. Quant. Spectrosc. Radiat. Transf. 257, 107738. https://doi.org/10.1016/j.jqsrt.2020.107338.

Shin, S., Noh, Y.M., Lee, K., Lee, H., Muller, D., Kim, Y.J., Kim, K., Shin, D., 2014. Retrieval of the single scattering albedo of Asian dust mixed with pollutants using lidar observations. Adv. Atmos. Sci. 31, 1417–1426. https://doi.org/10.1007/s00376-014-3244-y.

Stein, A.F., Draxler, R.R., Rolph, G.D., Stunder, B.J.B., Cohen, M.D., Ngan, F., 2015. NOAA's HYSPLIT atmospheric transport and dispersion modeling system. Bull. Am. Meteorol. Soc. 96, 2059–2077. https://doi.org/10.1175/BAMS-D-14-00110.1.

Sun, H., Wang, S., Hu, X., Liu, H., Zhou, X., Huang, J., Cheng, X., Sun, F., Liu, Y., Liu, D., 2022. Detection of surface defects and subsurface defects of polished optics with multisensor image fusion. PhotoniX 3, 6. https://doi.org/10.1186/s43074-022-00051-7.

Tatarov, B., Müller, D., Noh, Y.-M., Lee, K.-H., Shin, D.-H., Shin, S.-K., Sugimoto, N., Seifert, P., Kim, Y.-J., 2012. Record heavy mineral dust outbreaks over Korea in 2010: two cases observed with multiwavelength aerosol/depolarization/Raman-quartz lidar. Geophys. Res. Lett. 39, L14801. https://doi.org/10.1029/2012GL051972.

Tesche, M., Ansmann, A., Müller, D., Althausen, D., Engelmann, R., Hu, M., Zhang, Y., 2007. Particle backscatter, extinction, and lidar ratio profiling with Raman lidar in south and north China. Appl. Opt. 46, 6302–6308. https://doi.org/10.1364/AO.46.006302.

Tesche, M., Ansmann, A., Müller, D., Althausen, D., Engelmann, R., Freudenthaler, V., Groß, S., 2009. Vertically resolved separation of dust and smoke over Cape Verde using multiwavelength Raman and polarization lidars during Saharan mineral dust experiment 2008. J.Geophys.Res.Atmos. 114, D13202. https://doi.org/10.1029/2009JD011862.

Toll, V., Christensen, M., Quaas, J., Bellouin, N., 2019. Weak average liquid-cloud-water response to anthropogenic aerosols. Nature 572, 51–55. https://doi.org/10.1038/s41586-019-1423-9.

Uno, I., Eguchi, K., Yumimoto, K., Takemura, T., Shimizu, A., Uematsu, M., Liu, Z., Wang, Z., Hara, Y., Sugimoto, N., 2009. Asian dust transported one full circuit around the globe. Nat. Geosci. 2, 557–560. https://doi.org/10.1038/ngeo583.

Veselovskii, I., Goloub, P., Podvin, T., Bovchaliuk, V., Derimian, Y., Augustin, P., Fourmentin, M., Tanre, D., Korenskiy, M., Whiteman, D., Diallo, A., Ndiaye, T., Kolgotin, A., Dubovik, O., 2016. Retrieval of optical and physical properties of African dust from multiwavelength Raman lidar measurements during the SHADOW campaign in Senegal. Atmos. Chem. Phys. 16, 7013–7028. https://doi.org/10.5194/acp-16-7013-2016.

Wang, N., Shen, X., Xiao, D., Veselovskii, I., Zhao, C., Chen, F., Liu, C., Rong, Y., Ke, J., Wang, B., Liu, D., 2021a. Development of ZJU high-spectral-resolution lidar for aerosol and cloud: feature detection and classification. J. Quant. Spectrosc. Radiat. Transf. 261, 107513. https://doi.org/10.1016/j.jqsrt.2021.107513.

Wang, Z., Liu, C., Dong, Y., Hu, Q., Liu, T., Zhu, Y., Xing, C., 2021b. Profiling of dust and urban haze mass concentrations during the 2019 National Day Parade in Beijing by polarization Raman lidar. Remote Sens. 13, 3326. https://doi.org/10.3390/rs13163326.

Wang, N., Xiao, D., Veselovskii, I., Wang, Y., Russell, L.M., Zhao, C., Guo, J., Li, C., Gross, S., Liu, X., Ni, X., Tan, L., Liu, Y., Zhang, K., Tong, Y., Wu, L., Chen, F., Wang, B., Liu, C., Chen, W., Liu, D., 2022a. This is FAST: multivariate Full-permutAtion based Stochastic foresT method—improving the retrieval of fine-mode aerosol microphysical properties with multi-wavelength lidar. Remote Sens. Environ. 280, 113226. https://doi.org/10.1016/j.rse.2022.113226.

Wang, N., Zhang, K., Shen, X., Wang, Y., Li, J., Li, C., Mao, J., Malinka, A., Zhao, C., Russell, L.M., Guo, J., Gross, S., Liu, C., Yang, J., Chen, F., Wu, L., Chen, S., Ke, J., Xiao, D., Zhou, Y., Fang, J., Liu, D., 2022b. Dual-field-of-view high-spectral-resolution lidar: simultaneous profiling of aerosol and water cloud to study aerosol-cloud interaction. Proc. Natl. Acad. Sci. 119, e2110756119. https://doi.org/10.1073/pnas.2110756119.

Wei, J., Li, Z., Xue, W., Sun, L., Fan, T., Liu, L., Su, T., Cribb, M., 2021. The China high PM10 dataset: generation, validation, and spatiotemporal variations from 2015 to 2019 across China. Environ. Int. 146, 106290. https://doi.org/10.1016/j.envint.2020.106290.

Xiao, D., Wang, N., Shen, X., Landulfo, E., Zhong, T., Liu, D., 2020. Development of ZJU high-spectral-resolution lidar for aerosol and cloud: extinction retrieval. Remote Sens. 12, 3047. https://doi.org/10.3390/rs12183047.

Xie, C., Nishizawa, T., Sugimoto, N., Matsui, I., Wang, Z., 2008. Characteristics of aerosol optical properties in pollution and Asian dust episodes over Beijing, China. Appl. Opt. 47, 4945–4951. https://doi.org/10.1364/AO.47.004945.

Yin, Z., Wan, Y., Zhang, Y., Wang, H., 2021. Why super sandstorm 2021 in North China. Natl. Sci. Rev. 9, nwab165. https://doi.org/10.1093/nsr/nwab165.

Yu, X., Lü, R., Liu, C., Yuan, L., Shao, Y., Zhu, B., Lei, L., 2017. Seasonal variation of columnar aerosol optical properties and radiative forcing over Beijing, China. Atmos. Environ. 166, 340–350. https://doi.org/10.1016/j.atmosenv.2017.07.011.

Zhang, Z.L., Gao, Y., Li, X.J., Wang, X., Zhao, S.Y., Liu, Q., Zhao, C.M., 2022. Second harmonic generation of laser beams in transverse mode locking states. Adv.Photon. 4, 026002. https://doi.org/10.1117/1.Ap.4.2.026002.

Zhang, T., Zheng, M., Sun, X., Chen, H., Wang, Y., Fan, X., Pan, Y., Quan, J., Liu, J., Wang, Y., Lyu, D., Chen, S., Zhu, T., Chai, F., 2023. Environmental impacts of three asian dust events in the northern China and the northwestern Pacific in spring 2021. Sci. Total Environ. 859, 160230. https://doi.org/10.1016/j.scitotenv.2022.160230.

Zheng, Y., Che, H., Xia, X., Wang, Y., Yang, L., Chen, J., Wang, H., Zhao, H., Li, L., Zhang, L., Gui, K., Yang, X., Liang, Y., Zhang, X., 2021. Aerosol optical properties and its type classification based on multiyear joint observation campaign in North China Plain megalopolis. Chemosphere 273, 128560. https://doi.org/10.1016/j.chemosphere.2020.128560.

Zhong, T., Wang, N., Shen, X., Xiao, D., Xiang, Z., Liu, D., 2020. Determination of planetary boundary layer height with lidar signals using maximum limited height initialization and range restriction (MLHI-RR). Remote Sens. 12, 2272. https://doi.org/10.3390/rs12142272.